RI 9505

REPORT OF INVESTIGATIONS/1994

A Field Test of Electromagnetic Geophysical Techniques for Locating Simulated In Situ Mining Leach Solution

By D. R. Tweeton, J. C. Hanson, M. J. Friedel, B. K. Sternberg, and L. J. Dahl

UNITED STATES DEPARTMENT OF THE INTERIOR

BUREAU OF MINES

U.S. Department of the Interior
Mission Statement

As the Nation's principal conservation agency, the Department of the Interior has responsibility for most of our nationally-owned public lands and natural resources. This includes fostering sound use of our land and water resources; protecting our fish, wildlife, and biological diversity; preserving the environmental and cultural values of our national parks and historical places; and providing for the enjoyment of life through outdoor recreation. The Department assesses our energy and mineral resources and works to ensure that their development is in the best interests of all our people by encouraging stewardship and citizen participation in their care. The Department also has a major responsibility for American Indian reservation communities and for people who live in island territories under U.S. administration.

Report of Investigations 9505

A Field Test of Electromagnetic Geophysical Techniques for Locating Simulated In Situ Mining Leach Solution

By D. R. Tweeton, J. C. Hanson, M. J. Friedel, B. K. Sternberg, and L. J. Dahl

UNITED STATES DEPARTMENT OF THE INTERIOR
Bruce Babbitt, Secretary

BUREAU OF MINES

International Standard Serial Number
ISSN 1066-5552

CONTENTS

ILLUSTRATIONS

ILLUSTRATIONS—Continued

TABLES

UNIT OF MEASURE ABBREVIATIONS USED IN THIS REPORT

A	ampere	mrad	milliradian
A/m	ampere per meter	ms	millisecond
°C	degree Celsius	mS/m	millisiemens per meter
gal	gallon	μV/A	microvolt per ampere
gal/min	gallon per minute	mγ	milligamma
g/L	gram per liter	mγ/A	milligamma per ampere
H/m	henry per meter	rad	radian
Hz	hertz	rad/s	radian per second
kHz	kilohertz	s	second
km	kilometer	S/m	siemens per meter
L	liter	V/A	volt per ampere
L/min	liter per minute	V/m	volt per meter
m	meter	γ	gamma
m^2	square meter	$\Omega \cdot m$	ohm meter
min	minute		

A FIELD TEST OF ELECTROMAGNETIC GEOPHYSICAL TECHNIQUES FOR LOCATING SIMULATED IN SITU MINING LEACH SOLUTION

By D. R. Tweeton,[1] J. C. Hanson,[2] M. J. Friedel,[3] B. K. Sternberg,[4] and L. J. Dahl[5]

ABSTRACT

The U.S. Bureau of Mines, the University of Arizona, Sandia National Laboratories, and Zonge Engineering and Research Organization, Inc., conducted cooperative field tests of six electromagnetic (EM) geophysical methods to compare their effectiveness in locating a brine solution simulating in situ leach solution or a high-conductivity plume of contamination. The brine was approximately 160 m below the surface. The testsite was the University's San Xavier experimental mine near Tucson, AZ. Geophysical surveys using surface and surface-borehole, time-domain electromagnetic (TEM) induction; surface controlled-source audiofrequency magnetotellurics (CSAMT); surface-borehole, frequency-domain electromagnetic (FEM) induction; crosshole FEM; and surface magnetic field ellipticity were conducted before and during brine injection. The surface TEM data showed a broad decrease in resistivity. CSAMT measurements with the conventional orientation did not detect the brine, but measurements with another orientation indicated some decrease in resistivity. The surface-borehole and crosshole methods located a known fracture and other fracture zones inferred from borehole induction logs. Surface magnetic field ellipticity data showed a broad decrease in resistivity at depth following brine injection.

[1]Research physicist, Twin Cities Research Center, U.S. Bureau of Mines, Minneapolis, MN.
[2]Geophysicist, BHP Minerals, Herndon, VA.
[3]Geophysicist, Twin Cities Research Center.
[4]Head, Department of Mining and Geologic Engineering, University of Arizona, Tucson, AZ.
[5]Geologist, Twin Cities Research Center.

INTRODUCTION

Certain oxide ore deposits, such as porphyry coppers, may be amenable to in situ mining (*1*).[6] In situ mining depends on the dissolving action of an infiltrating leach solution. The leach solution, often a dilute solution of water and sulfuric acid, is injected into the deposit, usually through a surface injection well. After permeating the ore, the leach solution is recovered through production wells located elsewhere on the surface or in underground mine openings. In situ leaching offers potential economic advantages over conventional surface or underground mining techniques. These advantages include elimination or reduction of the need for excavation, blasting, crushers, concentrators, and haulers. Thus, in situ mining may allow profitable production from lower grade ore. In addition, miner safety is improved because of reduced dependence on an underground labor force.

The leach solution selectively attacks oxide mineralization hosted in fractures or other areas accessible to solution flow. The amount of metal that is actually dissolved is highly dependent on the extent of contact between leach solution and oxide mineralization. This contact is directly related to the location and depth of the injection and production wells with respect to fracturing.

Obtaining knowledge before in situ mining of fracture systems that can control most of the fluid flow is an essential but difficult and expensive undertaking. An extensive drilling program is usually required to properly assess ore grades and tonnages, mineralogy, and chemistry, as well as fluid flow and fracture characteristics. While some of this developmental drilling cannot be avoided, geophysical methods can be used to position some wells to improve injection, production, or monitoring processes. The cost of locating fractured zones could be significantly reduced by eliminating unnecessary drilling.

Fracture detection by electromagnetic (EM) methods can be greatly enhanced if fractures have been saturated with conductive material, such as conductive ground water (*25*) or leach solution (*16*). Acid leach solutions are highly conductive and, like any fluid, will preferentially follow paths of least resistance, such as fractures. Hence, the presence of leach solution will indicate the presence of fractures in crystalline rock. In porous rocks, such as sandstone, flow is more uniformly distributed throughout the rock mass and fractures may be difficult to detect.

Accurate location of fracture systems is also important for environmental monitoring of leach solution flow. Leach solution that escapes the well field may pose an environmental threat to aquifers. EM methods could be used to map the location and depth of conductive leach solution, providing valuable information to mining companies and regulatory agencies, and could provide an early warning of flow away from the area of containment. Furthermore, geophysical methods for monitoring leach solution have the potential to help determine if leach solution is being distributed to all portions of the deposit. Thus, the U.S. Bureau of Mines (USBM) conducted this research as part of its effort to reduce costs, enhance mining productivity, and improve safety.

Several EM methods appeared promising for conductive fluid detection, particularly time-domain electromagnetic (TEM) induction (*26*) and controlled-source audiofrequency magnetotellurics (CSAMT) (*47*). Although some of the methods had been used at various sites for different reasons, these methods had not been compared at one site under conditions sufficiently relevant to in situ mining. To evaluate and compare them adequately for applications in detecting and monitoring leach solution, it was necessary to use all the candidate methods at one site under the same conditions to map the same target.

In July 1990, a cooperative experiment involving the USBM, Sandia National Laboratories, and the University of Arizona was undertaken at the university's San Xavier experimental mine (*40*) (see figure 1) near Tucson. The experiment was designed to simulate in situ mining using

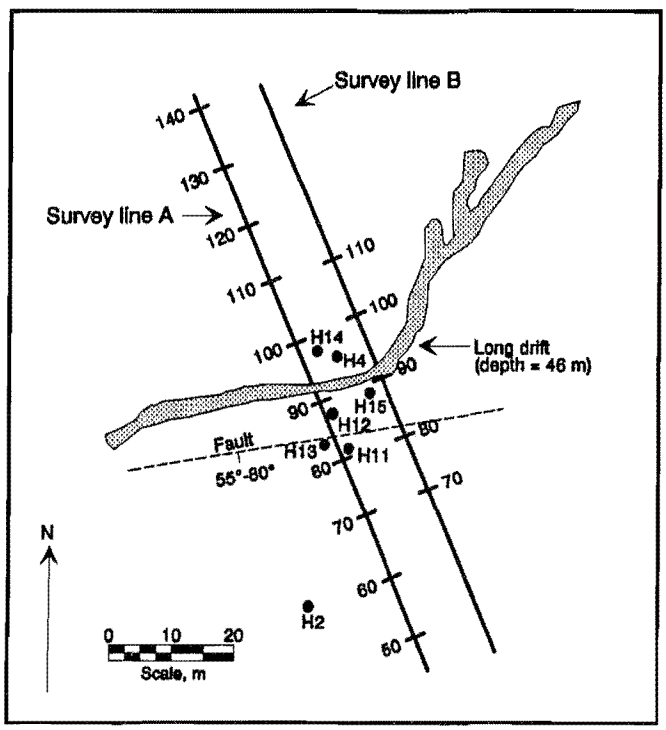

Figure 1.—Borehole locations (indicated by black circles) and geophysical survey lines.

[6]Italic numbers in parentheses refer to items in the list of references at the end of this report.

a conductive salt water plume as a geophysical target. Selected EM methods were systematically compared for their effectiveness in detecting the plume.

The USBM tested surface and surface-borehole TEM and CSAMT (surface-only method) methods. Sandia researchers tested surface-borehole and crosshole frequency-domain electromagnetic (FEM) induction. The USBM and Sandia hired Zonge Engineering and Research Organization, Inc., of Tucson, AZ, to conduct those geophysical surveys. The University of Arizona tested an internally developed surface FEM method described by Sternberg (*37*) for measuring the magnetic field ellipticity. The university also measured the conductivity of rock near boreholes with a borehole induction logging tool. The tested methods had been selected as the most promising for detecting deeply injected, low-resistivity solutions in rocks having relatively low resistivity (*16*).

Prior to the cooperative experiment, an environmental permit for the brine injection, required by Arizona environmental authorities, was obtained by the University of Arizona. Permit approval required demonstration of aquifer protection and daily ground water sampling to show that metals were not being leached from the rock and mobilized by the brine solution. An important advantage of performing the experiment cooperatively was that all of the participants could benefit from the permitting effort of the university.

Various geophysical methods were previously tested at the San Xavier site (*40*). These methods include seismic refraction, dc resistivity, induced polarization, and CSAMT. The intent of these surveys was to characterize rock properties and to provide a data base from which subsequent surveys could be designed. In addition, crosshole tunnel detection experiments used the long exploration drift shown in figure 1 as a target (*45*).

The experiment is relevant to numerous applications, such as monitoring acid mine drainage, detecting fractures for engineering or site characterization studies, and investigating fluid contamination at hazardous wastesites. EM techniques that measure the conductivity of the subsurface or the conductance (conductivity times thickness) of objects within the subsurface are used for engineering and hazardous waste studies (*15, 25, 28*) and ground water exploration (*13, 24, 30*). A few studies discuss the potential of EM methods for the detection of leach solution plumes, including those by Hanson (*16*) and Tweeton (*42*). Zonge (*47*, p. 806) discussed a successful application of CSAMT for detecting leach solution. Several researchers have demonstrated successful application of dc resistivity in salt water injection experiments (*6, 46*).

This report provides a detailed description of the experiment. To facilitate comparing the geophysical methods, this report describes the equipment for all methods, then the data processing for all methods, and finally the results for all methods. The availability of data not used in this report is pointed out because they may be of value to other researchers. These data may be requested from Tweeton. Additional information about the surface-borehole and crosshole FEM tests is given by Lee (*23*). Shorter publications that summarize the findings have been published previously (*17-18*).

ACKNOWLEDGMENTS

The authors thank Kenneth L. Zonge, president, Zonge Engineering and Research Organization, Inc., Tucson, AZ, and Zonge Engineering for their valuable expertise and technical support throughout the experiment and during the writing of this report. Many of the results and conclusions are the direct result of comments and suggestions from Zonge and Zonge Engineering.

In addition, the authors thank the University of Arizona at Tucson for its many contributions. The USBM is grateful to Ben K. Sternberg, professor, Department of Mining and Geological Engineering, University of Arizona, for permission to use the San Xavier mine as an experimental testsite. The discussion of the University of Arizona's experiment with magnetic field ellipticity was contributed by Sternberg. We thank Jon Benedict, graduate student, Hydrology Department, University of Arizona, for contributing data from borehole EM induction logs. A special thanks goes to Stacy Bohannon, graduate student, also of the Hydrology Department, for her patience and persistence in obtaining the aquifer protection permit. Daily water sampling, mandated by the permit, was conducted by Bohannon during the injection process.

The authors also thank Sandia National Laboratories researchers David O. Lee and J. Robert Wayland for their important contributions to the success of the downhole FEM tests. These contributions include providing downhole equipment made for Sandia by Zonge Engineering, collecting much of the downhole data, and correcting the problem of electrical noise from the pipeline corrosion protection system.

SITE GEOLOGY

The survey area lies in a faulted and metamorphosed sequence of Paleozoic and Mesozoic rocks with locally high fracture permeability (*40*). The predominant lithology around the injection boreholes is Permian Concha limestone that is in fault contact with the Cretaceous Angelica arkose. The Concha limestone is medium to dark gray, crystalline, and contains abundant chert that occurs as nodules ranging in size from a few centimeters to a half meter. It is host to much of the lead and zinc skarn (contact metamorphic) mineralization in the area and locally strongly altered to garnetite. The Angelica arkose is thin bedded and consists of subangular to well-rounded quartz and feldspar grains. Figure 2 shows the geologic logs from portions of three of the boreholes shown in figure 1, based on information provided by Sternberg (*40*).

The test area is cut by a normal fault that strikes N. 80° E. to N. 90° E. and dips 55° to 80° to the south, roughly parallel to bedding. The Angelica arkose lies south of the fault and limestones and garnetites lie to the north. Joint orientation data shown in figure 3 were collected by the USBM on surface outcrops and adapted from Sternberg (*40*) for underground mine workings at the adit level, the 30-m level, and the 46-m level. A primary joint set, identified from the underground workings, strikes approximately N. 45° E. and dips 60° to 78° southeast. Two minor joint sets observed at the 46-m level strike N. 22° E. and dip 50° northwest, and strike N. 83° E. and dip 39° southeast, respectively. Joint orientations measured on surface outcrops near the survey area primarily strike N. 38° E. and dip 72° northwest. These northeast-striking, southeast- and northwest-dipping conjugate joint sets are generally consistent with the known regional geologic fabric of Arizona (*19*) and expected to be consistent at the injection depth.

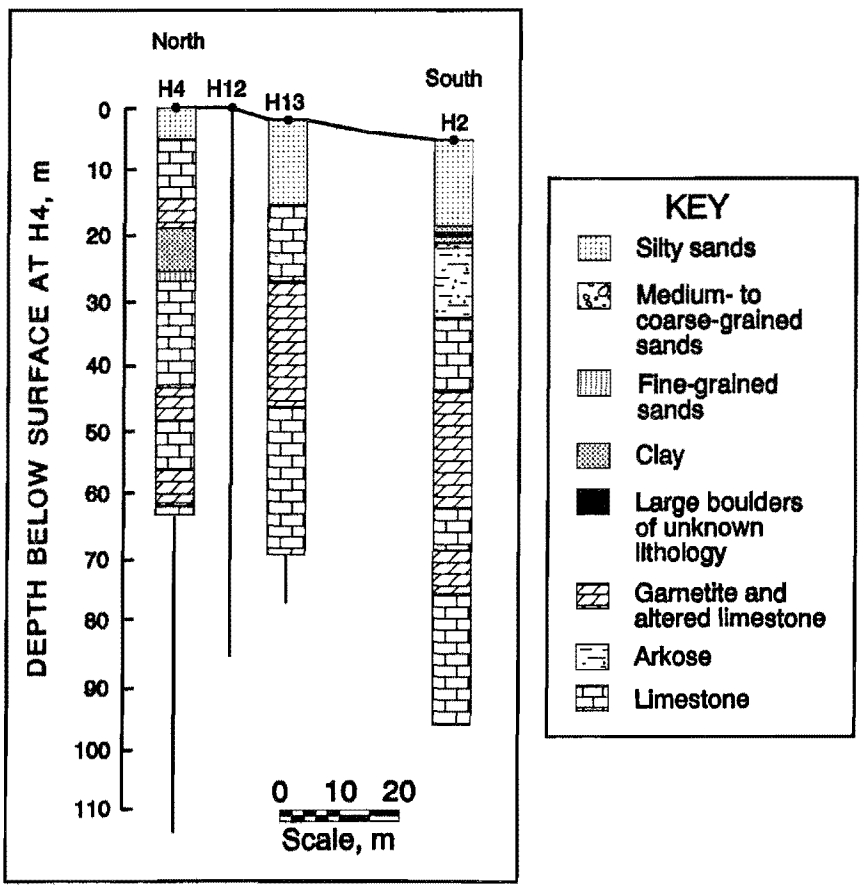

Figure 2.—Borehole geologic logs. [Adapted from Sternberg (*40*).]

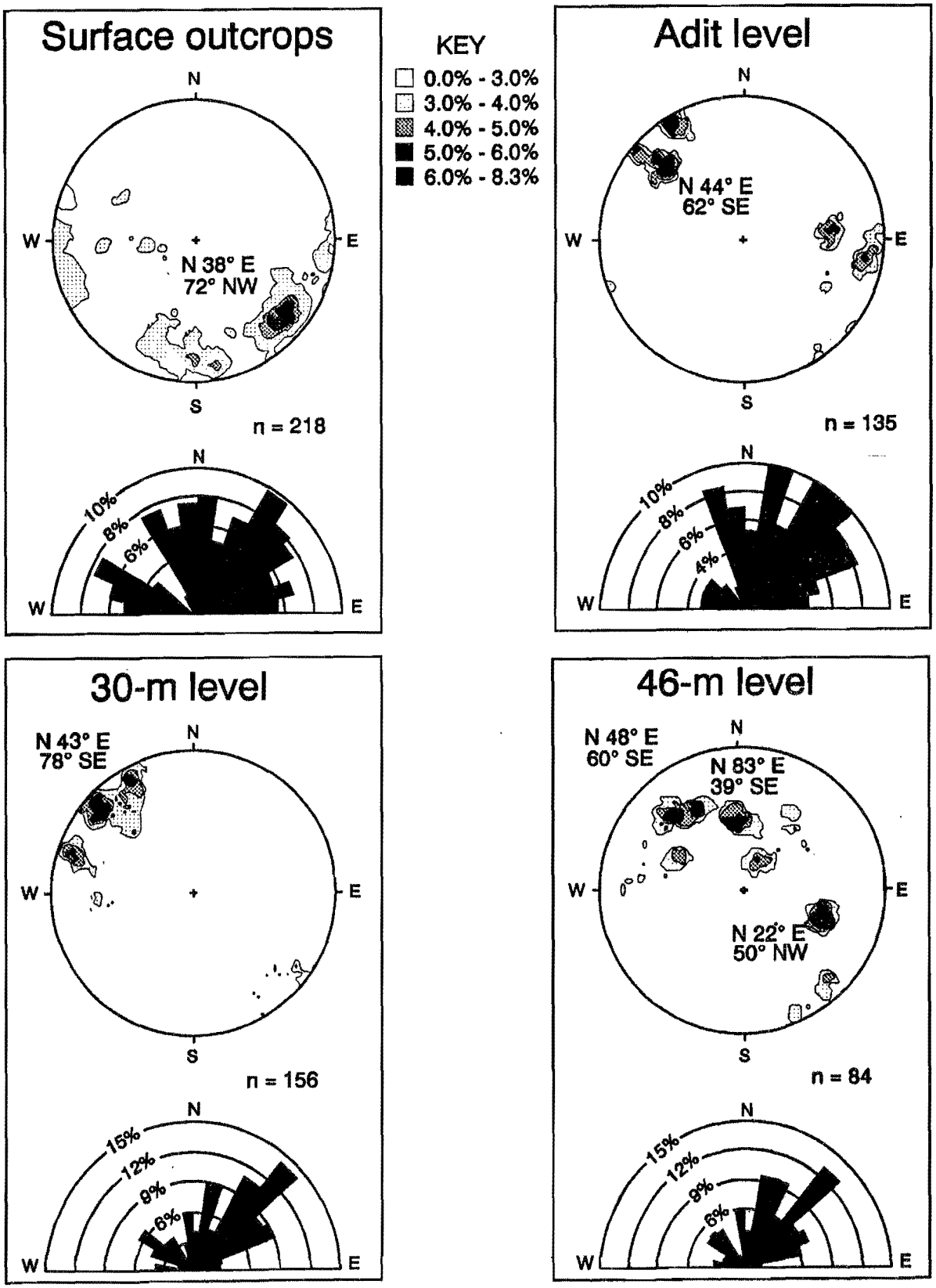

Figure 3.—Schmidt equal area projections and strike frequency rosettes for joints. [Adapted from Sternberg (*40*).]

GENERAL EXPERIMENTAL PROCEDURE

Figure 1 is a plan view of the survey lines and boreholes. The primary survey line was A. Budget constraints allowed only limited data collection along line B to investigate both sides of the injection wells. These parallel survey lines were 10 m apart and oriented N. 30° W. with 10-m survey station intervals.

Figure 4 provides a perspective view of the boreholes and shows that the depth of the boreholes was considerably greater than the distance between them. All boreholes were cased with polyvinyl chloride that does not affect EM data. Borehole deviation surveys showed that the deviations from vertical were not significant for the purposes of this experiment.

Geophysical surveying was performed before and during injection to allow the effects of geology to be separated from those associated with the brine. The surface TEM and CSAMT surveys were conducted before injecting brine, repeated while injecting brine in borehole H4, and repeated again while injecting brine in both H4 and H15. The surface magnetic field ellipticity surveys were conducted before injection and repeated while injecting in both H4 and H15. Surface-borehole and crosshole surveys were conducted before injection and while injecting brine into H4. H14 was the primary borehole for environmental monitoring, but was also used in the borehole geophysical surveys.

The brine contained 23 g/L NaCl, based on the weight of salt added to a known volume of water. The brine was made by adding salt to municipal water trucked to the site from the nearby town of Green Valley, south of Tucson, AZ, and mixing the solution in two 2,300-L (600-gal) fiberglass tanks. The brine had a resistivity of 0.28 Ω•m (a conductivity of 3.6 S/m), corrected to 25° C, which provided a conductivity over 100 times that of the country rock.

The resistivity of the brine was higher than that of leach solution planned for copper in situ leaching. Discussions with experts and unpublished information indicate that in situ copper leaching solution will probably contain about 10 to 25 g/L H_2SO_4. Sulfuric acid of 10.0 and 25.4 g/L has resistivities of 0.21 and 0.088 Ω•m (conductivities of 4.8 and 11.3 S/m), respectively (*10*). Thus, EM methods that detected the brine solution at 160 m should be more sensitive to copper in situ leach solution at a comparable depth.

A total of 110,000 L (29,000 gal) of solution was injected 30 m above the 157-m deep water table. Brine was injected in borehole H4 during the one-well injection at about 30 L/min (8 gal/min), and in H4 and H15 at 15 to 19 L/min (4 to 5 gal/min) in each borehole during the two-well injection. The wells were not pressurized. Over the 8-day injection period, 68,000 L (18,000 gal) was injected during the one-well test and 42,000 L (11,000 gal) during the two-well test. The one-well injection was longer because all of the borehole measurements and many of the surface measurements were conducted during this test. The two-well test was intended to produce two plumes to provide an additional spatial resolution test for the surface EM methods. However, it was not possible to verify whether two plumes were actually developed and two plumes could not be interpreted from the geophysical data.

The effective depth was less than the drilled depth for some boreholes because of infilling sediment. Effective

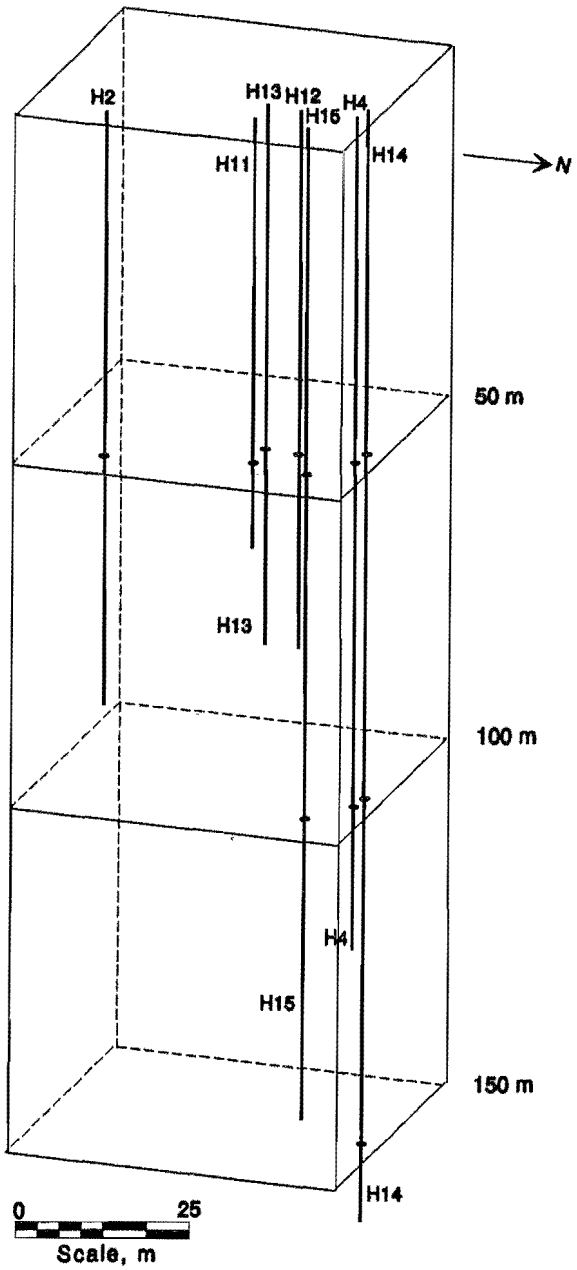

Figure 4.—Perspective view of boreholes.

depths were 128 m (injection borehole H4), 131 m (injection borehole H15), and 159 m (borehole H14). The water table was at a depth of 157 m in H14. During injection, some of the brine flowed from H4 to H14, a surface distance of 3.2 m, through a large fracture at a depth of 120 m. The unsealed receiver probe, located at a depth of 120 m in H14, once became saturated and inoperable, providing direct evidence of this fracture zone. Other fracture zones were inferred from borehole induction logs.

Although not confirmed, 120 m below surface was the inferred maximum height to which injection borehole H4 could be filled. At depths less than 120 m, brine rapidly drained out of the borehole, which prevented measuring the maximum fluid level. Unfortunately, it was not possible to measure fluid level while injecting brine; however, measurements made immediately after stopping injection were never less than 120 m. Based on this information, it was inferred that brine was entering fractures intercepted by H4 between depths of 120 m and the bottom of the borehole, or 128 m.

From this interval, brine probably flowed almost straight down until reaching the water table because of the extensive fracturing. It could then continue downward because the brine was denser than ground water. It could also spread somewhat to the south or southeast because of the combination of south-southeast dipping joints and the hydraulic gradient created by the injection process. Brine could also spread to the northeast or southwest along the strike of the joints.

In the second injection borehole (H15), information about the injection interval was more difficult to obtain because brine left the borehole as fast as it was injected, preventing any measurement of the level of brine. The simplest assumption was that brine was entering the formation at the bottom of the borehole. No communication, via fractures, could be established between injection boreholes H4 and H15. The exploration drift at a depth of 46 m had no apparent effects on the surface or borehole results.

The volume of the brine target was small relative to the depth. Injection did not continue overnight, so brine injected one day may not have contributed fully to the target for the next day because of a combination of mixing with the ground water and/or sinking below the zone of interest. The extent of the plume in the fractured rock is unknown, since it would depend on the connected porosity and fracture pattern of the rock. However it was distributed, the small amount of brine in the effective target provided a challenging test for the sensitivity of these EM methods.

EQUIPMENT AND MEASUREMENTS

The data for all of the EM tests except surface magnetic field ellipticity were collected on a Zonge Engineering multipurpose GDP-16[7] data acquisition system. Data were stacked and averaged to reduce effects from noise. Surface measurements were usually taken at 10-m intervals. Most borehole data were collected at intervals of 3 or 1.5 m.

For both surface and downhole measurements, the three components of the induced magnetic field were measured with three orthogonal coils. The sensitivity of a coil to an induced magnetic field is governed by its effective area—that is, the area times the number of turns of wire times a factor for the effect of core material, if not air. The effective area of each of the three surface receiver coils for the TEM and CSAMT methods was 10,000 m^2, while the areas of the downhole coils were 130 m^2 for the two horizontal components and 400 m^2 for the vertical component. The smaller effective areas of the downhole coils negated to some extent the advantage of being closer than the surface coils to the region of interest.

In the following discussions, the X direction is horizontal and perpendicular to the survey lines, Y is parallel to the survey lines, and Z is vertical. Thus, H_z is the vertical magnetic field, and E_y is the electric field parallel to the survey lines.

TIME-DOMAIN ELECTROMAGNETIC METHOD

The surface TEM transmitter and receiver configuration used in this test is shown in figure 5. The transmitter loop was an ungrounded square, 200 m on each side, with two sides parallel to the survey lines. The loop size was chosen to obtain adequate depth of penetration. The loop, centered about the injection boreholes, was energized by a 10-A, 32-Hz bipolar step current (square wave) operating at a duty cycle of 50%. This wave form was provided by a Zonge Engineering GGT-30 constant-current transmitter.

The transient voltages induced in each of the three orthogonal receiver coils were measured as a function of time after the current in the transmitter loop was turned off. When the transmitter is turned off, the change in the EM field induces eddy currents in conductive material. These eddy currents diffuse downward with increasing time and induce voltages in the receiver coils (*27*, pp. 428-430). This method is convenient because no electrical contact

[7]Reference to specific products does not imply endorsement by the U.S. Bureau of Mines.

with the ground is needed. The transient voltage decay curve was sampled at 22 logarithmically spaced time intervals or channels, with increasing times corresponding to increasing depths of investigation.

In most commercial surveys, only H_z is measured, which is adequate when imaging a one-dimensional (1-D) layered geology. Measuring H_x and magnitude of Y-directed magnetic field (H_y), in addition to H_z, gave additional useful data, as will be discussed in the "Results" section.

All measurements were made inside the one fixed transmitter loop. This arrangement is called the in-loop configuration. Other configurations are possible, depending on the application and objective. Data interpretation is simpler for surveys inside a loop, since the field is more symmetric with respect to the receiver. Furthermore, logistics are easier if the loop is large enough so it does not have to be moved during the survey.

The configuration for the surface-borehole (transmitter on surface, receiver in borehole) TEM surveys is shown in figure 6. The signal source was the same 200-m square loop used for the surface surveys. All measurements were taken in boreholes near the center of the loop, using a

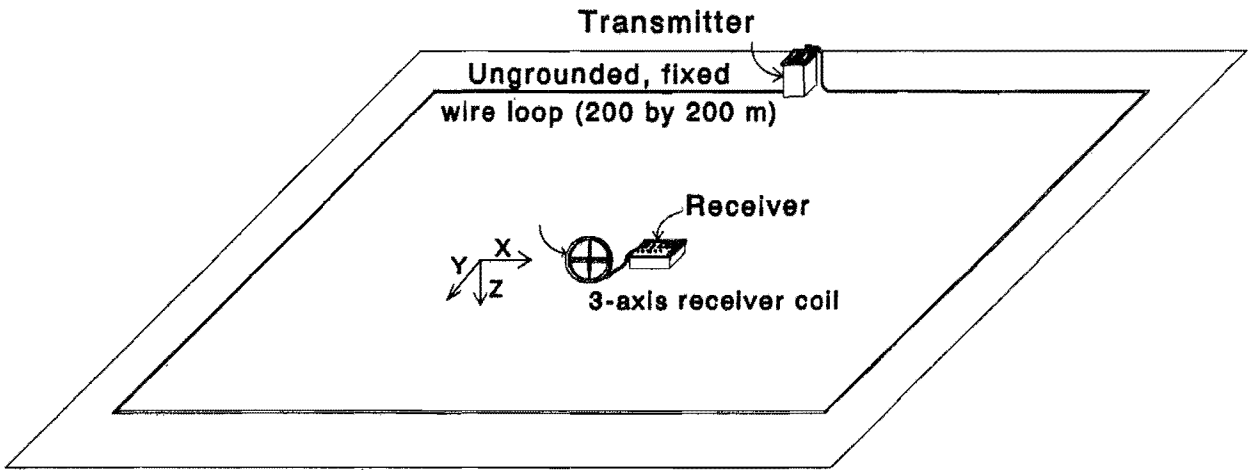

Figure 5.—Surface TEM configuration of transmitter and receiver. (Survey lines are in Y direction.)

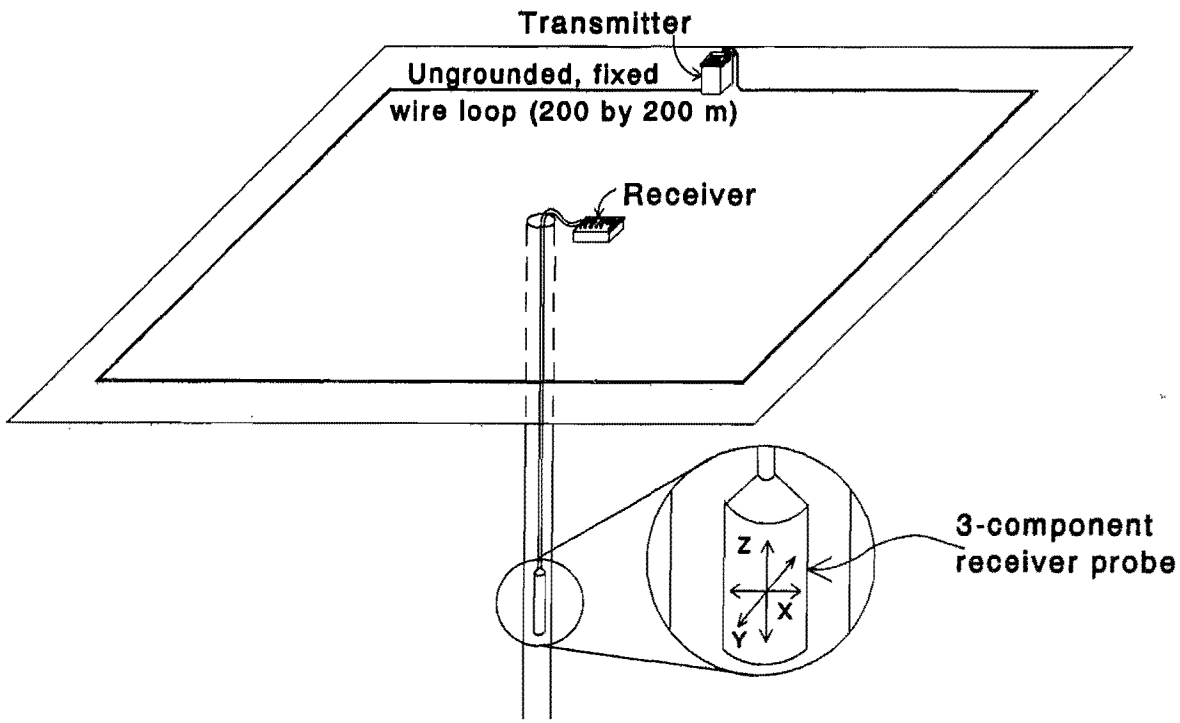

Figure 6.—Surface-borehole TEM configuration of transmitter and receiver.

prototype receiver described by Lee (*23*). An electronic compass, attached to the receiver housing and interfaced with a surface computer, was used to monitor azimuthal changes as the probe was raised or lowered. No directional information is available for the preinjection TEM horizontal components because the communication software for the receiver probe was not delivered until after the surface-borehole preinjection TEM data had been collected. The compass readings were not used in the analysis for this report, but are available from Tweeton.

Surface-borehole TEM measurements were recorded as a function of depth in boreholes H12, H14, and H15 (injection borehole) before and during injection in H4. The depth ranges for these measurements are shown in table 1. Measurements were recorded at intervals of 1.5 or 3 m, the latter used near the top of the boreholes where the brine had less effect. The receiver would not drop below 93 m in H15. The injection survey in H12 was started at 61 instead of 25 m to save time. The injection survey in H14 was stopped at 128 m because brine flowing into H14 through the large fracture at 120 m damaged the probe.

Table 1.—Surface-borehole TEM ranges of depths in boreholes at which data were recorded, in meters

Borehole	Preinjection	Injection
H12	25- 78	61- 79
H14	85-146	61-128
H15	61- 93	61- 91

CONTROLLED-SOURCE AUDIOFREQUENCY MAGNETOTELLURICS

The configuration of the transmitter and receiver for CSAMT is shown in figure 7. The transmitter dipole was 450 m long and grounded at both ends. It was 1.8 km south-southeast of the injection area and oriented N. 80° E., or about 20° off perpendicular from the survey lines. The transmitter should be far from the receiver to avoid near-field effects that reduce the reliability of resistivity calculations. A GGT-30 transmitter supplied 13 A to the dipole source. The frequencies used were 64, 128, 256, 512, 1,024, 2,048, 4,096, and 8,192 Hz.

Unlike the TEM method, CSAMT requires grounded dipoles for recording the electric field, in addition to coils for recording the magnetic field. The magnitude of X-directed electric field (E_x) and E_y were measured with 10-m dipoles, grounded with porous pots. The vertical component is very small and normally not measured. H_x, H_y, and H_z were measured with the same coils used for the surface TEM method. The GDP-16 system recorded the two electric dipole voltages, the voltages induced in the three receiver coils by the magnetic field, the phase angles between transmitted and received electric fields, and the phase angles between transmitted and received magnetic fields. The usual practice in CSAMT is to measure only E_x and H_y, but E_y and H_x were also measured to determine if they would be useful.

FREQUENCY-DOMAIN ELECTROMAGNETIC METHOD

The surface-borehole FEM survey configuration is shown in figure 8. The transmitter dipole was 610 m long, oriented normal to the survey lines, and grounded at both ends. It was located at station position 0 m, about 95 m south of injection borehole H4. The three magnetic field components were measured at the 128-Hz fundamental frequency and its first four odd harmonics (384, 640, 896, and 1,152 Hz) and also at the 1,024-Hz fundamental frequency and its first four odd harmonics (3,072, 5,120, 7,168, and 9,216 Hz) with the same three-axis borehole probe used for the surface-borehole TEM method.

Preinjection measurements were recorded over most of the length of borehole H12, H14, and H15 (injection borehole). During injection, time constraints limited data collection to the lower portion of the boreholes. The depth ranges for these measurements are shown in table 2.

Table 2.—Surface-borehole FEM ranges of depths in boreholes at which data were recorded, in meters

Borehole	Preinjection	Injection
H12	25- 79	61- 79
H14	30-146	114-146
H15	45- 91	61- 91

Crosshole FEM tests (see figure 9) were conducted between borehole H14 and injection borehole H15, 10 m apart. The borehole transmitter (*23*), containing a slim vertical-axis coil, was set at 125 and 130 m in H15 while the receiver depth in H14 was varied. The transmitter was of smaller diameter than the receiver and did not stop at 93 m in H15, as the receiver had done. Measurements were recorded at the 1,024-Hz fundamental frequency and its first four odd harmonics with the same downhole receiver. Measurements could not be recorded at 128 Hz because of the high background noise level.

SURFACE MAGNETIC FIELD ELLIPTICITY

A high-resolution EM sounding system, developed at the University of Arizona's Laboratory for Advanced Subsurface Imaging (LASI), was also used to record field

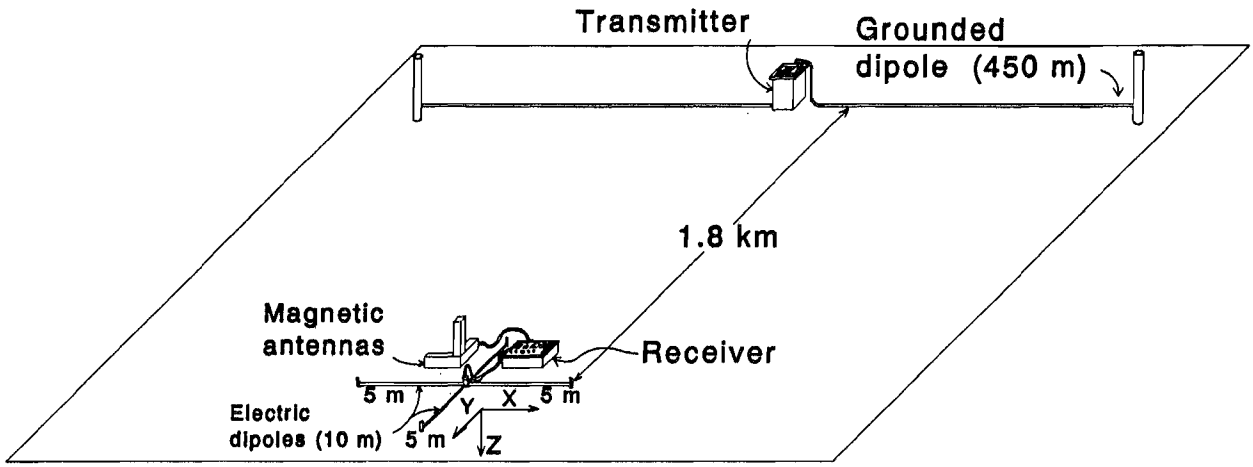

Figure 7.—CSAMT configuration of transmitter and receiver. (Survey lines are in Y direction.)

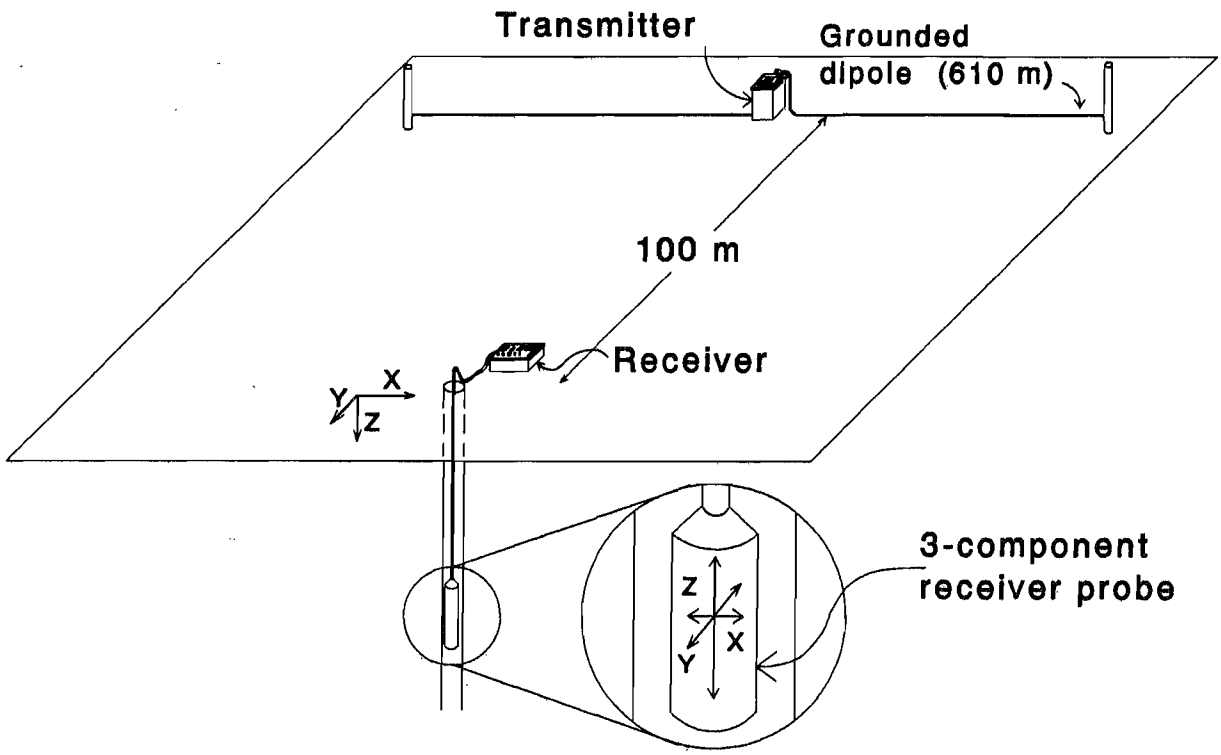

Figure 8.—Surface-borehole FEM configuration of transmitter and receiver.

data. The LASI high-resolution EM system incorporates several new features, including high-accuracy calibration (*37*, *39*) and mathematical rotation of three-dimensional (3-D) measured EM fields (*3*). The system was designed to record ellipticity of the magnetic field at receiver sites located near a source transmitting a swept-frequency waveform. The system has a wide bandwidth (30 Hz to 30 kHz) and can rapidly record stations at a high spatial sampling density (essentially continuous profiling). A detailed description of the LASI high-resolution ellipticity system was given by Sternberg (*37*).

A schematic of the ellipticity measuring system is shown in figure 10. The transmitter consists of the power amplifier placed in line with a 610-m long transmitter wire that discharged approximately 1 A of current into the ground. This transmitter wire was the same dipole used for the surface-borehole FEM surveys, located at station position 0 m. The current from this transmitter induces a

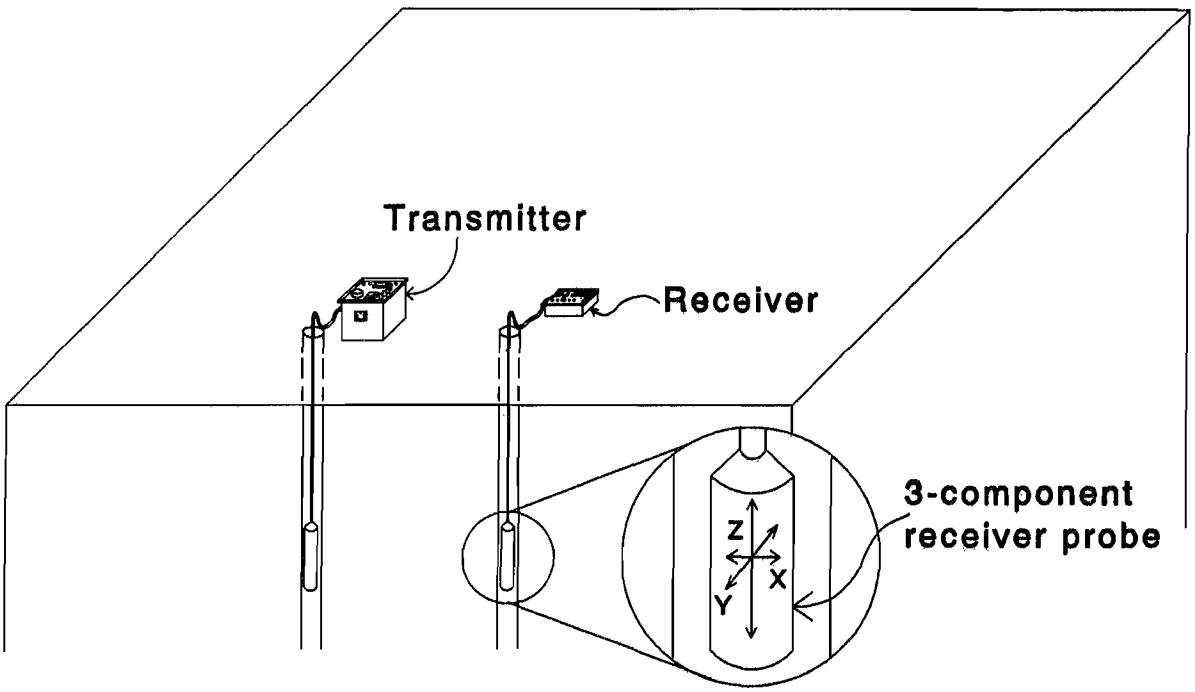

Figure 9.—Crosshole FEM configuration of transmitter and receiver.

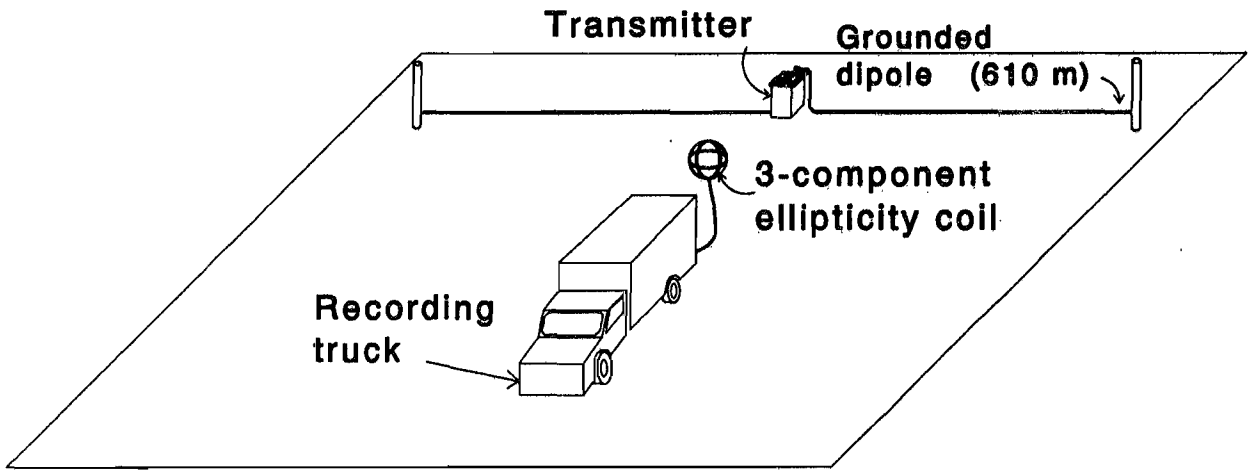

Figure 10.—Surface magnetic field ellipticity configuration of transmitter and receiver.

secondary electric and magnetic field in the plume of injected brine. A receiver, consisting of three orthogonal coils of wire approximately 0.75 m in diameter with a calibration coil at 54.7° to each, was used to measure the total magnetic field in three directions at each station along a traverse over the injection region. A suite of 19 frequencies (29, 58, 87, 116, 145, 204, 320, 465, 698, 988, 1,450, 2,150, 3,140, 4,650, 6,800, 10,000, 14,700, 21,600, and 31,600 Hz) was swept at each survey station to obtain a depth sounding. Data were recorded at 10-m intervals along line A from 60 to 130 m before and during the two-well injection.

DATA PROCESSING

Data processing techniques can be applied to reduce effects from topography and atmospheric or cultural noise, in addition to calculating resistivity and other parameters of interest. Surface TEM, CSAMT, and magnetic field

ellipticity data are often displayed as contoured resistivity cross sections using the "apparent resistivity" (*35*) and the "apparent depth." These parameters are calculated using simplifications, such as assuming that resistivity is uniform down to the apparent depth. Such cross sections are known as pseudosections because the relationship between resistivity and depth is a complicated function of resistivity distribution and measurement technique, as well as the method of data processing. Hence, the depths and resistivities indicated on pseudosections are not necessarily correct. Resistivity pseudosections are sometimes used to construct an image of the geologic cross section by a process called inversion (*36*).

TIME-DOMAIN ELECTROMAGNETIC METHOD

Unprocessed TEM data consist of the normalized voltages induced in the receiver coils at time channels or windows after transmitter turnoff. The voltages are normalized by dividing by the transmitter loop current. The normalized voltages induced on the vertical receiver coil at position 100 m on line A are shown in figure 11. This type of curve is called a decay plot or sounding because increasing time corresponds to increasing depth.

Resistivity measurements from TEM surveys are not subject to the static effects that can affect CSAMT results because the electric field is not measured. However, being a broadband system, the TEM method may be more susceptible than CSAMT to electrical noise sources such as cables, powerlines, pipelines, and thunderstorms.

Unprocessed preinjection TEM data contained electrical noise. The effects of noise are evident in figure 11, where the late-time data appear to oscillate. This position was selected for display because it shows an unusually high noise level. The preinjection data were recorded while the cathodic protection (to prevent corrosion) for a nearby buried gas pipeline was energized. Zonge (*47*, p. 736) states that pipelines are one of the worst sources of cultural noise, especially with cathodic protection. The cathodic protection was turned off later, which reduced the noise by a factor of 10 at 1,024 Hz during preinjection FEM surface-borehole measurements. It remained off during brine injection. Thunderstorms may also have contributed to the noise by affecting the late-time, weaker TEM signals.

The more strongly affected late-time data were smoothed, and the smoothed data were used to recalculate resistivity and depth values. Most data were smoothed by a modified three-point running average or by averaging affected data with nearby unaffected data. Frequency-domain notch filtering was tried, but introduced too much ringing. Data recorded during injection were not smoothed because they were not adversely affected by thunderstorms or other electrical activity.

The filtering and smoothing made the late-time results more consistent with site information and with the injection resistivities at large depths. However, the smoothing had little effect on the resistivities at the depths of interest because, for typical resistivities found with the TEM system, the depths of interest corresponded to earlier time channels than were seriously affected by the noise. For example, an apparent depth of 250 m with a uniform resistivity of 100 $\Omega \cdot$m corresponds to only 0.8 ms. These results demonstrate that TEM data may require special care regarding electrical noise, especially if late-time data are needed for large depths of penetration.

Apparent resistivities were calculated from the normalized voltages with the 1-D modeling program RHOTEM. The program was adapted by Zonge Engineering from a program published by the New Jersey Geological Survey (*32*). The program calculates resistivities and depth from the Z-component voltage response of in-loop sounding, with a square loop. It uses an early- and a late-time asymptotic approximation to the resistivity as initial guesses in an iterative calculation of resistivity for times between early and late. The program can calculate the voltage corresponding to a specified resistivity at a specified time channel. Thus, for each time channel, the program calculates iteratively the resistivity corresponding to the observed voltage for that time. The program provides a ramp correction because the turnoff of a transmitter loop is not instantaneous, but decreases nearly linearly over a short time (*12*). This ramp time was 0.075 ms.

The early-time asymptotic approximation for apparent resistivity (ρ_a) was

$$\rho_a = (v/3M)(L/\sqrt{\pi})^3, \qquad (1)$$

where v = receiver voltage at t divided by transmitter current before turnoff, V/A,

M = effective area (area multiplied by number of turns multiplied by core material factor) of receiver coil, m^2,

L = transmitter loop side length, m,

and π = 3.1416.

The late-time asymptotic approximation was

$$\rho_a = 6.322 \times 10^{-12} L[(L)(M/tv)^2]^{1/3}/t, \qquad (2)$$

where t = time channel, s.

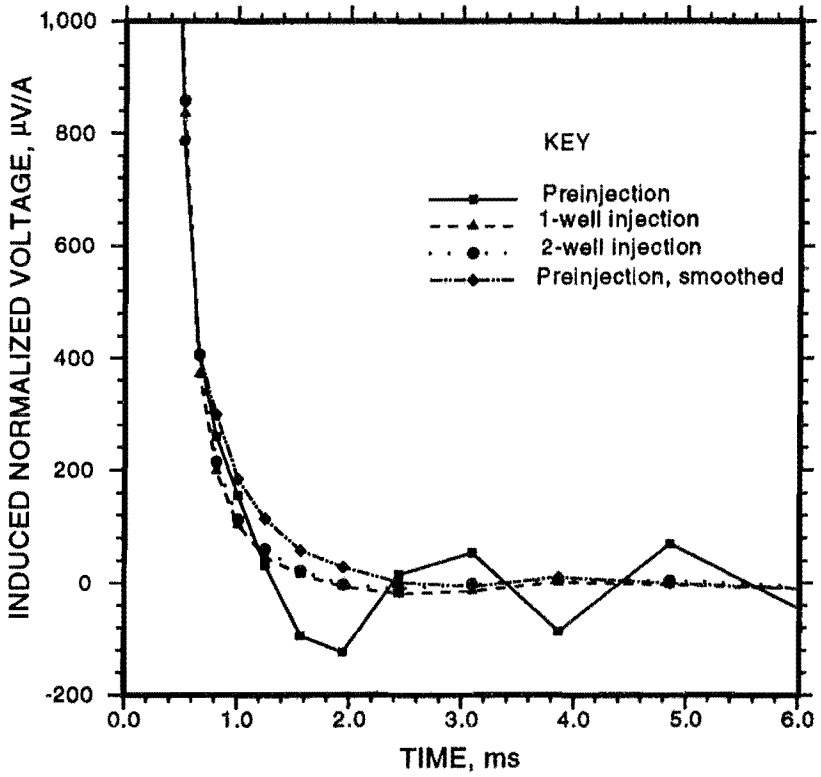

Figure 11.—TEM decay plot, Z component, at 100-m station on line A, showing noise at late times.

The formula for apparent depth in the same program is

$$D_{app} = 28(\rho_a t)^{1/2}, \quad (3)$$

where D_{app} = apparent depth, m,

and t = time channel, ms.

The apparent resistivities would be correct only if the resistivities were uniform. A Niblett-Bostick inversion (*8, 22, 29*) was applied to the apparent resistivities to improve the reliability of the results by considering layering. (The Niblett-Bostick inversion was first developed for frequency-domain applications, but can be applied equally well to time-domain applications with time channels analogous to frequencies. The inversion uses the change in apparent resistivity with frequency or time channel to calculate a correction for each apparent depth and resistivity.) The program is 1-D, however, so the calculated depth and resistivity are not necessarily the correct values. Like apparent resistivity, the calculation of depth in TEM measurements may be affected by the degree of anisotropy and the noise level.

The surface horizontal components were not directly inverted to calculate separate resistivity pseudosections, but provided valuable additional information, as explained in the "Results" section.

Just as for surface TEM data, surface-borehole data consisted of the voltage induced in three orthogonal coils as a function of time after turning off the current in the transmitter loop. The normalized voltages were expressed as microvolts per ampere of transmitter loop current (μV/A) on voltage decay curves for each borehole depth. At each depth for each borehole, the μV/A response was recorded for each of the three orthogonal coils for each of the 22 time channels, from 0.038 to 6.098 ms. However, the data after 4 ms were noisy and were not used in the resistivity calculations. Time channels were not converted to apparent distance from the borehole because such a conversion would not be reliable. Furthermore, a useful comparison between preinjection and injection data does not require that conversion.

CONTROLLED-SOURCE AUDIOFREQUENCY MAGNETOTELLURICS

Resistivity estimates from CSAMT data are obtained from a ratio of the perpendicular electric and magnetic field values. When the transmitter is a sufficient distance from the receiver, apparent resistivities may be calculated from the Cagniard resistivity equation (*5, 9*):

$$\rho_a = (1/\omega\mu)(E_x/H_y)^2, \quad (4)$$

where ρ_a = apparent resistivity, Ω•m,

ω = 2πf, rad/s (π = 3.1416, rad, f = frequency, Hz),

μ = magnetic permeability in free space, $4\pi \times 10^{-7}$ H/m,

E_x = magnitude of X-directed electric field, V/m,

and H_y = magnitude of Y-directed magnetic field, A/m.

(Unless known, magnetic permeability is always assumed to be the free space (vacuum) value of $\mu = \mu_o = 4\pi \times 10^{-7}$ H/m.)

For field use, it is convenient to express the electric field in millivolts per kilometer and the magnetic field in gammas (1 γ = 0.01/4π A/m). Then equation 4 becomes (*47*, p. 723)

$$\rho_a = (1/5f)(E_x/H_y)^2. \quad (5)$$

Under certain conditions (*47*), equation 4 or equation 5 can be used equally well with E_y and H_x. However, experience has shown that deviations from a homogeneous or horizontally layered earth environment will cause significant differences between E_x/H_y (also called transverse magnetic) and E_y/H_x (transverse electric) resistivity calculations (*4*, *47*). Hence, the presence of two-dimensional (2-D) or 3-D structures may impose limitations on the accuracy of the resistivity calculations as well as the depth at which they are interpreted to occur. With sufficient data, 2-D and 3-D computer modeling could improve the reliability of the results.

The calculated apparent depth corresponding to a given apparent resistivity and frequency is the "effective" exploration depth in CSAMT surveying.

$$D_{eff} = 356(\rho_a/f)^{1/2}, \quad (6)$$

where D_{eff} = effective depth, m.

D_{eff} is 71% of the skin depth. Skin depth is defined as the distance a wave will penetrate before attenuating to 1/e (37%) of its original amplitude (*33*). If the subsurface resistivity were uniformly 60 Ω•m (a typical resistivity for the CSAMT data) and the CSAMT frequencies ranged from 8,192 to 64 Hz, then the minimum and maximum effective exploration depths would be 30 and 340 m, respectively.

CSAMT depths for contouring resistivities were calculated by applying a 1-D Niblett-Bostick inversion (*8*, *22*, *29*) to the Cagniard apparent resistivities. In most places, including the San Xavier testsite, resistivities vary horizontally, violating the assumptions of a 1-D layered resistivity. Consequently, the depth calculated with the Niblett-Bostick inversion is not necessarily the true depth.

Phase data are usually recorded simultaneously with electric and magnetic magnitude data in CSAMT surveys (*47*). Electric field phase (E_ϕ) is a measure of the phase angle between the transmitted and received electric field signals in the same direction (X or Y). Likewise, magnetic field phase (H_ϕ) is a measure of the phase angle between the transmitted and received magnetic field signals in the same direction. Phase difference (ϕ) is the difference between the electric and magnetic phases.

In a layered earth, phase difference is a function of resistivity layering. The phase difference is related to the derivative of the logarithm of the resistivity with respect to the logarithm of the angular frequency:

$$\phi = E_\phi - H_\phi = (\pi/4)(1 + \partial\ln\rho/\partial\ln\omega). \quad (7)$$

Equation 7 shows that values higher than π/4 indicate high-over-low-resistivity layering while values lower than π/4 indicate low-over-high-resistivity layering. Therefore, phase difference is useful for indicating changes in resistivity with depth. In a homogeneous environment, the logarithmic term equals zero and $\phi = \pi/4$ rad = 45° = 785 mrad.

Phase data can also be helpful in correcting static effects. Static effects, also called static shift or offset, cause the resistivity sounding curves, derived from electric and magnetic field magnitudes, to be shifted up or down from their true values (*47*), but do not affect phase differences. The effect on calculated resistivity is due to charge distribution at the boundaries of shallow 2-D and 3-D bodies altering the electric field measurements. The effect on the magnetic field values is negligible. All geophysical methods that make use of the electric field are subject to static effects to some degree.

Static effects are common in CSAMT data and, if not properly corrected, will yield erroneous resistivity and depth information. Several static correction techniques are described by Zonge (*47*, pp. 763-766). Practical methods include (1) CSAMT data processing, such as phase integration and spatial filtering; and (2) comparison with independent, static-free measurements.

Phase integration, applied in this experiment, uses the static-free phase difference data to calculate phase-derived resistivity data for each measurement station. All such resistivity values are normalized by ρ_N, a normalizing resistivity chosen from a particular frequency and measurement station (reference station) believed to be unaffected by

static shift. In a similar manner, a reference phase (ϕ_r) is selected from the same data set. The static-corrected resistivity from phase difference values is then obtained from the following formula:

$$\rho_{stat} = \rho_\phi(\rho_N/\rho_{ref})\exp[(4/\pi)(\phi_r - \phi_s)], \quad (8)$$

where ρ_{stat} = static-corrected resistivity, Ω•m,

ρ_N = normalizing resistivity, Ω•m,

ρ_{ref} = resistivity at reference frequency for each station, Ω•m,

ϕ_r = reference phase, mrad,

ϕ_s = phase at all stations and frequencies except reference station, mrad,

and

$$\rho_\phi = \rho_N \exp[(-4/\pi)\int_{f_L}^{f_H}(\phi - \pi/4)d\ln f], \quad (9)$$

where f_H, f_L = highest and lowest survey frequencies, respectively.

The measured ρ_a can sometimes be used in place of ρ_ϕ to simplify the static correction procedure.

All San Xavier CSAMT data were corrected for static shift by Zonge Engineering using this method. The validity of this method depends on the choice of normalizing resistivity and reference phase values from assumed static-free data. In applying equations 8 and 9, the following normalizing values were used: ρ_N = 63 Ω•m and ϕ_r = 785 mrad. The 63 Ω•m was an average surface resistivity obtained from the TEM data. This value was used for ρ_N to make it easier to compare the TEM and CSAMT data. The normalizing frequency was 4,096 Hz. The static corrections were applied to the 4,096 Hz data, and the rest of the sounding was scaled from that point.

Another CSAMT data processing technique—spatial filtering—depends on static effects due to local (small scale) sources compared to the size of the survey area. In this way, the local (affected) resistivity curves can be normalized to large scale curves that are more representative of background (unaffected) areas (*7, 37-38, 44*).

An alternative static correction technique uses independent static-free measurements for comparison with the CSAMT data. For example, Sternberg (*41*) applied TEM measurements to static-shift corrections for MT data. This type of correction was not used in the San Xavier experiment, however. Under many instances, static-free independent data may not be available, and additional geophysical surveying may increase the total cost of the geophysical program. For leach solution monitoring, rapid surveying is advantageous to minimize the effect of mining-induced changes during the survey, such as alterations in injection or recovery rates or depths. Therefore, the extra time required for additional surveys, especially if performed at a later date, may reduce the effectiveness of the static correction.

FREQUENCY-DOMAIN ELECTROMAGNETIC METHOD

In the FEM surface-borehole technique, raw H_z data, plotted as a function of borehole depth, were satisfactory for locating fractures containing brine. In addition, the horizontal components provided an opportunity to investigate a novel technique for detecting leach solution. In conventional surface-borehole surveys, the horizontal components are rarely measured because of the limited availability of three-component probes, or because of directional uncertainty in the orientation of the probe. Rather than attempt to rotate the probe and monitor its azimuth, it is simpler to employ a technique that allows the data to be used independently of coil orientation. Such a technique, called ellipticity, is related to the parameters of the polarization ellipse (*14*).

Ellipticity in any plane is the complex ratio of the minor and major axes of the polarization ellipse and related to conductivity. The parameters of the ellipse in the horizontal plane can be determined from the magnitudes and phases of the two horizontal components if they remain horizontal. Since the boreholes were very nearly vertical, the coil axes remained very nearly horizontal. These surface-borehole ellipticities were displayed directly, rather than calculating resistivities as was done for the surface magnetic ellipticity data.

The FEM crosshole raw H_z data were simply plotted as a function of receiver depth. The data readily indicated the presence of brine without further processing.

SURFACE MAGNETIC FIELD ELLIPTICITY

Hoversten (*21*), Ryu (*31*), and Smith (*34*) have concluded that magnetic ellipticity is a sensitive descriptor of ground conductivity and target depth. The polarization ellipse can be described by field components H_r (vector sum of H_x plus H_y) and H_z or by ellipse parameters e (ellipticity) and α (tilt angle), such that

$$e = \left|\frac{H_2}{H_1}\right| = \left|\frac{H_z\cos\alpha - H_r\sin\alpha}{H_z\sin\alpha + H_r\cos\alpha}\right| \quad (10)$$

and $$\tan(2\alpha) = \frac{2\left|\frac{H_z}{H_r}\right| \cos\left(\theta_z - \theta_r\right)}{1 - \left(\frac{H_z}{H_r}\right)}, \qquad (11)$$

where θ_z, θ_r = phases of vertical and horizontal components, respectively, of total field.

The University of Arizona's magnetic field ellipticity measurements were converted to an apparent-resistivity pseudosection. Apparent resistivities (in ohm meters) were calculated by finding, for each frequency and recording station, the homogeneous half-space resistivity yielding a calculated ellipticity equal to the observed ellipticity. The apparent resistivity pseudosection gives an estimate of the subsurface electrical resistivity structure.

The method of Anderson (*2*) was used for calculating the apparent resistivity corresponding to each observed ellipticity. Anderson's program was used in forward modeling to calculate the ellipticity corresponding to resistivities, and iterative calculations were performed to determine the resistivity corresponding to the observed ellipticity. Ward (*43*) describes the magnetic fields generated by sources of various configurations, including the grounded dipole used in this experiment. Frischknecht (*14*) describes the polarization ellipse.

An apparent depth scale was calculated from the plane-wave skin depth (using the calculated apparent resistivity at each measurement frequency) divided by 5. The scaling factor of 5 was chosen by comparing these skin depths with results from 1-D modeling. These scaled depths are not rigorous depth estimates. The apparent-resistivity pseudosection with its associated skin depth scale is, however, a convenient and effective means of displaying the data.

RESULTS

The success of the results depends on correlation with the known factors affecting expected fluid flow. As stated previously, flow was expected to be primarily downward, with some spreading toward the south after reaching the water table at 157 m. Spreading was also possible along the strike of permeable joints. In general, the results were consistent with the expected flow.

For both surface TEM and CSAMT methods, the one-well injection results were similar to the two-well results. Since the separation between the two injection boreholes was only 13 m and the depth of plume formation was 125 m or more, it is not surprising that two separate plumes could not be delineated. Both one-well and two-well injection results are displayed because the similarity of these results, obtained on different days, helps to demonstrate that the difference between preinjection and injection results was caused by the brine, not by day-to-day fluctuations unrelated to the injection.

SURFACE TIME-DOMAIN ELECTROMAGNETIC METHOD

The line A resistivity pseudosections for preinjection, one-borehole injection, two-borehole injection, and the change in resistivity from preinjection to two-well injection are shown in figure 12. The brine should decrease the resistivity. The preinjection resistivity data indicate a wide resistive layer, centered at about 210 m depth. The figures reveal a general decrease in resistivity with injection over most of line A at a calculated depth of 180 to 240 m, which is attributed to the brine. The width of a response to a subsurface conductor is similar to the depth (*27*, p. 459), so brine at the water table at 157 m or at the major fracture at 120 m should affect readings over most of the line. The narrow high-resistivity feature below the injection boreholes in the injection resistivity sections is attributed to a metallic object at the surface to the side of the survey line, as will be explained after the line B results are discussed. The general decrease in resistivity with injection showed that this method can detect brine at this depth, if lateral resolution similar to the depth of the conductor is adequate.

The limited data from line B for preinjection, one-well injection, and two-well injection are shown in figure 13. The one-well data were taken at fewer stations, but are similar to the two-well data at the same stations. The line B results were dominated by a strong, narrow resistivity decrease with injection between stations 90 and 100, consistent with the line A results. As will be shown, this result was probably caused by a surface metallic conductor rather than the brine.

The narrow resistivity changes below the injection wells seemed too narrow to be caused by the brine at depth. The horizontal components proved useful in identifying the cause. The horizontal and vertical normalized voltage changes are shown in figure 14, as two-well injection minus preinjection values. The time channels displayed correspond to calculated depths of 152 to 281 m, assuming a uniform resistivity of 100 Ω•m. This range demonstrates the slow decay of the induced signal. As shown in figure 14, the horizontal components showed sharp changes near

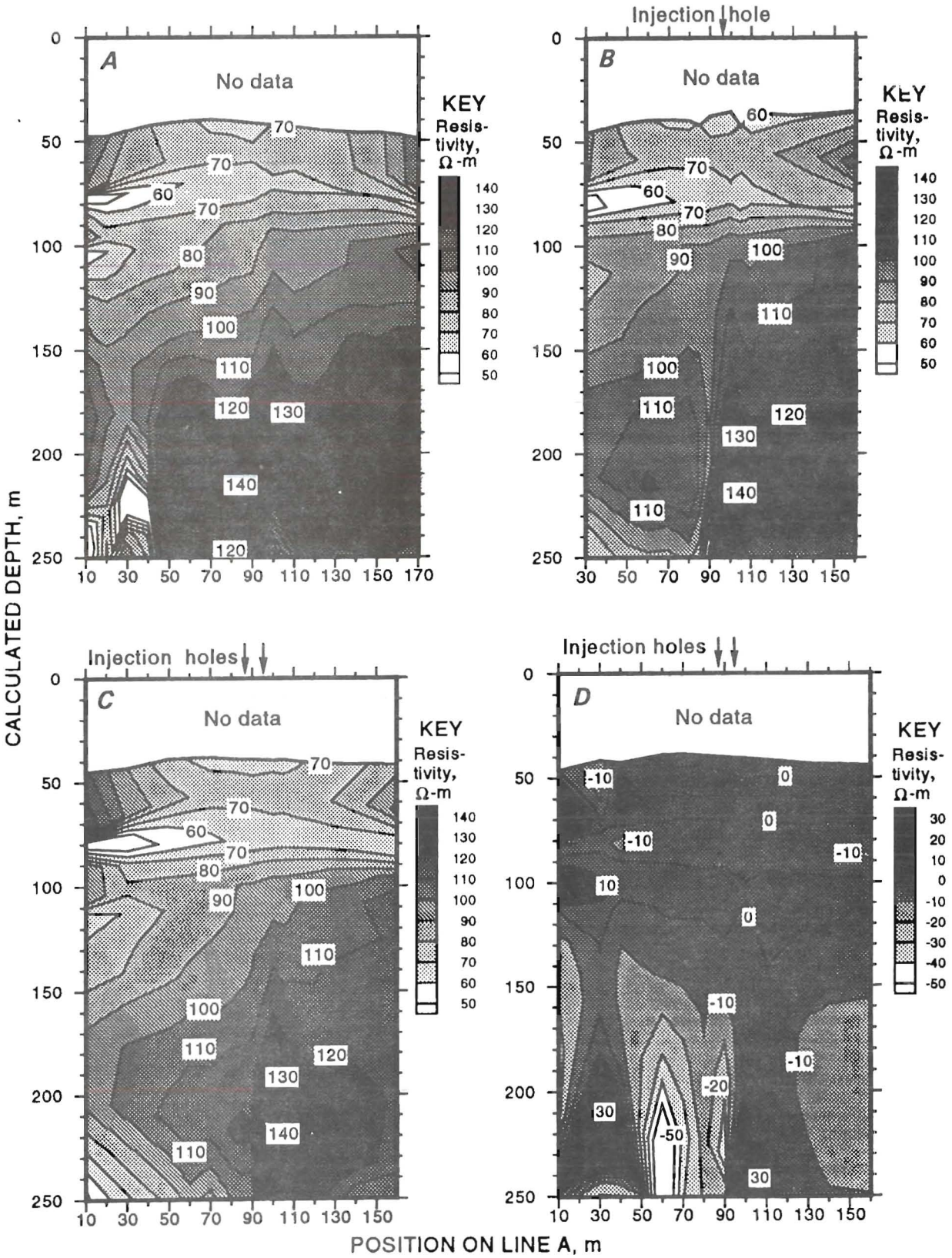

Figure 12.—TEM resistivity pseudosections, line A. *A*, Preinjection; *B*, one-well injection; *C*, two-well injection; *D*, two-well injection minus preinjection.

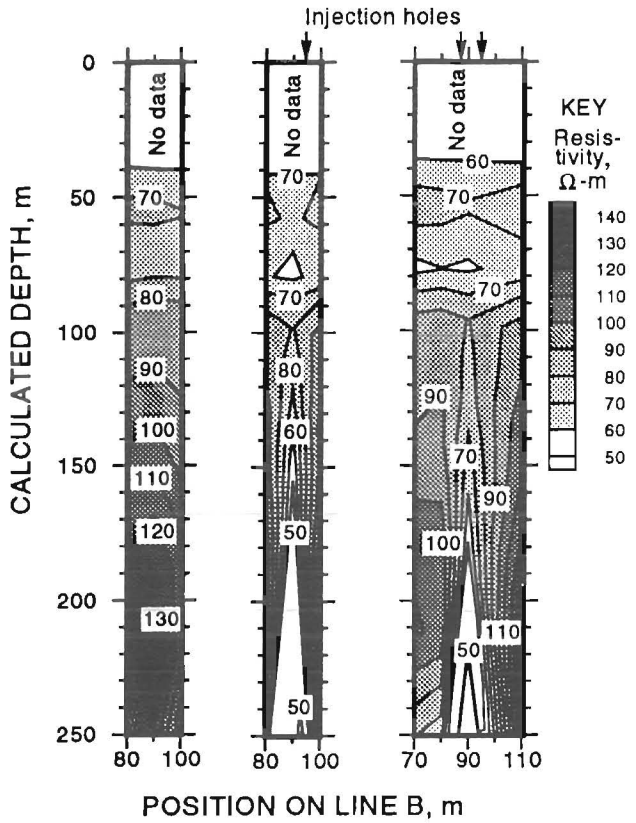

Figure 13.—TEM resistivity pseudosections, line B. Left, Pre-injection; center, one-well injection; right, two-well injection.

the injection boreholes. The Y-component (parallel to the survey line) change showed a narrow antisymmetric response near borehole H14. The antisymmetry showed that opposite ends of the Y-component coil pointed at the conductor as the survey moved past the conductor. The X-component change showed a narrow negative symmetric feature near H14. The symmetry showed that the same end of the X-component coil pointed at the conductor as the survey moved past the conductor, indicating that it was to the side of line A.

The narrowness of the horizontal component features are characteristic of a small near-surface conductor. A rule of thumb is that the depth (or conductor-receiver separation) is about the same as the half-width at half-maximum for a symmetric peak and half the distance between maximum and minimum values for an antisymmetric feature (*27*, p. 459), which implied that this conductor was no more than 10 m from the receiver.

The long time constant produced by the object indicated that it was a very good conductor, better than the brine. If an object can be approximated as a spherical conductor, the time constant (*27*, p. 467) is

$$\tau = \mu\sigma a^2/\pi^2, \qquad (12)$$

where σ = conductivity, S/m

and a = radius, m.

A metallic conductor has a conductivity σ of about 10 S/m, so a metallic conductor with a radius of 0.1 m has a time constant of 13 ms. The other surface conductors investigated were the mixing tanks for the brine. However, a tank of brine of conductivity σ of 3 S/m with a radius of 0.75 m has a time constant of 0.0002 ms, too short to be observed in even the earliest time window of 0.038 ms. The response was still strong at 1 ms, indicating the conductivity σ was that of a metal, not of the brine. The winch system used to hoist the water samples for the environmental sampling is the probable conductor because it was moved very close to line B between the preinjection and the injection surveys.

A narrow high-resistivity feature in the Z-component pseudosection for line A is plausible. A conductor at the side of the survey line could contribute a negative component to the vertical-induced magnetic field as magnetic lines from the conductor curve around it. The long time constant would make it appear deep in the pseudosection.

TEM resistivities show a depth to brine that is about 180 m, somewhat deeper than would be expected from the water table at 157 m. This result may be caused by inaccurate (1-D) TEM inversion and/or weak EM coupling due to the geometry of the transmitter-target-receiver combination. Problems with using 1-D interpretation methods with 2-D structure have been examined by Hoekstra (*20*). Hoekstra found that 1-D interpretation gave a general indication of the structure, but the values of the resistivity were not correct. Thus, the general pattern was useful, but the values of the resistivity could not be relied on directly to indicate rock type or the in situ conductivity of the solution.

SURFACE-BOREHOLE TIME-DOMAIN ELECTROMAGNETIC METHOD

The brine caused a significant change in the voltages and hence in the calculated apparent resistivity in borehole H14. However, no significant changes associated with injection were observed in borehole H12 and injection borehole H15. Those measurements were limited to shallow depths, well above the injection level because H12 was shallow and the receiver would not go below 93 m in H15. The data from H12 and H15 are not displayed, but are in data tables available from Tweeton.

The preinjection Z-component depth profiles of induced normalized voltage (receiver voltage/transmitter current) for seven time channels in borehole H14 before and during one-well injection are displayed in figure 15 as a function of depth. The seven channels shown cover a time

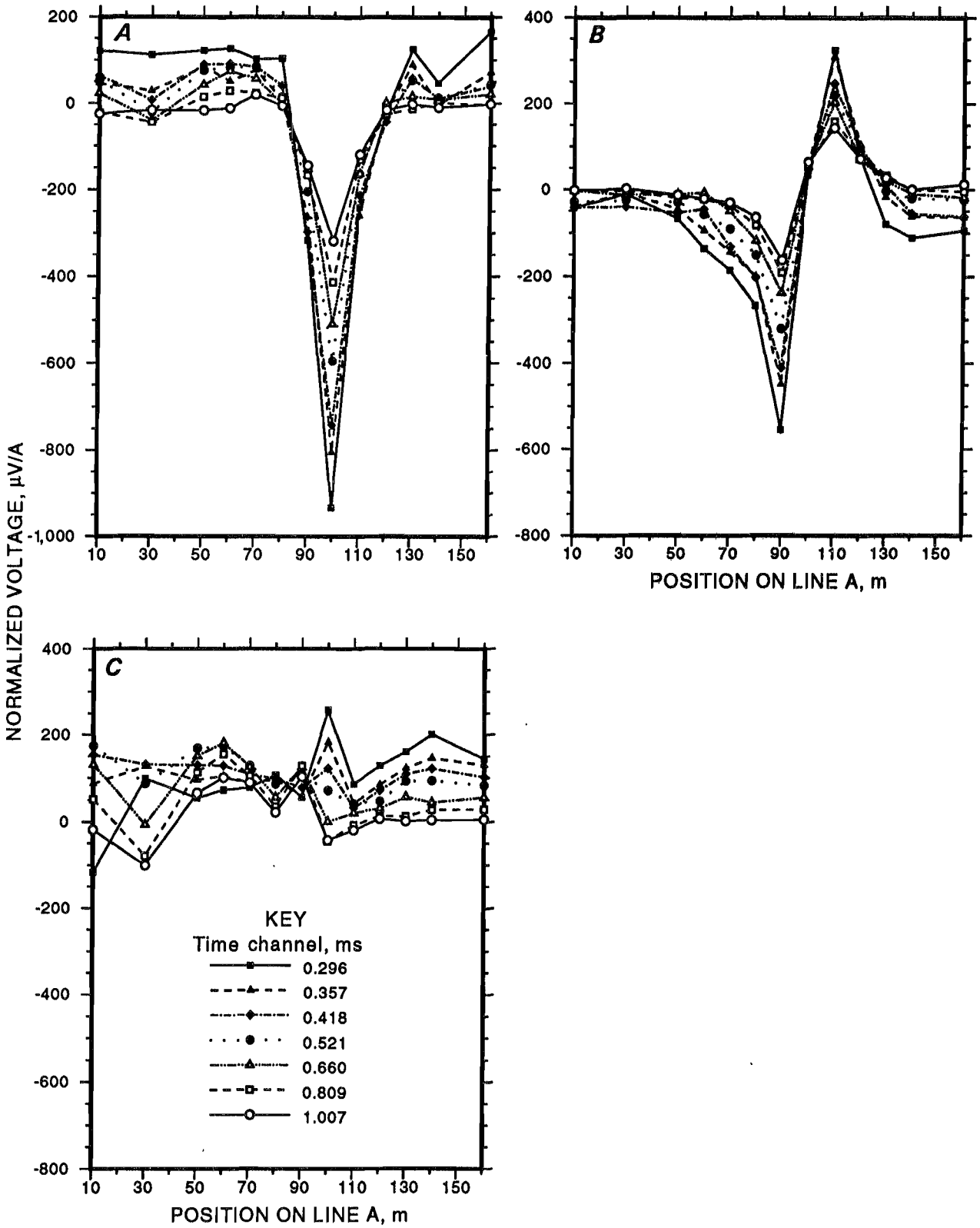

Figure 14.—TEM normalized voltage changes, two-well injection minus preinjection, line A. *A*, X component (perpendicular to survey line); *B*, Y component (parallel to survey line); *C*, Z component (vertical).

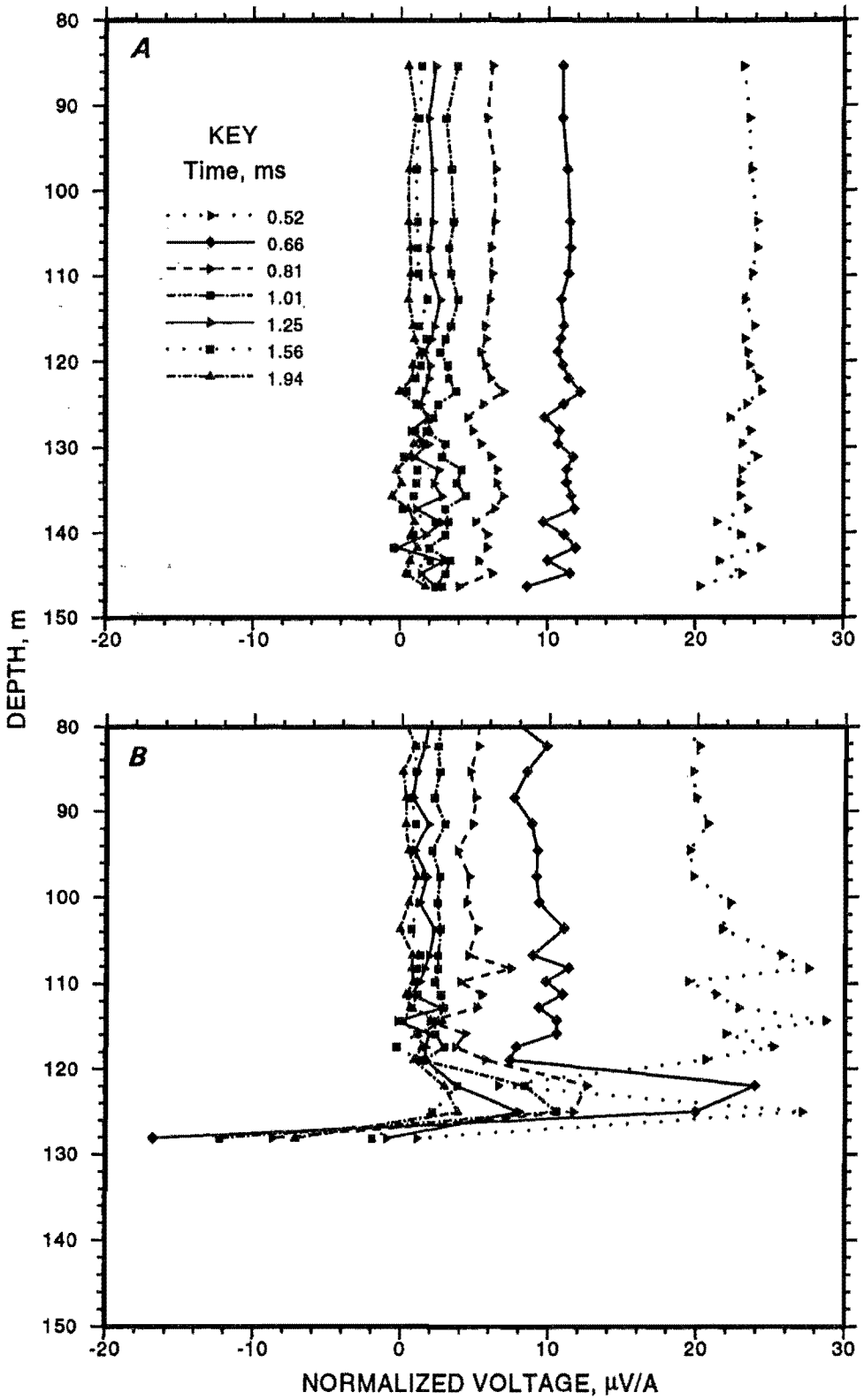

Figure 15.—Surface-borehole TEM Z component of normalized voltages in borehole H14. *A*, Preinjection; *B*, one-well injection.

range from about 0.5 to 2 ms after transmitter turnoff. The magnitudes show significant changes near 120 m related to injection. The preinjection data are quite smooth for all times, indicating no nearby strong conductors. A known permeable fracture zone, intercepted by both H4 (injection borehole) and H14 at a depth of 120 m, is not apparent in the preinjection data. The injection data contain a zero crossover near 120 m for the earliest time, which is probably related to injection. Other time channels show significant changes too. Data could not be recorded below 128 m because of the danger of damaging the unsealed probe.

This type of display allows the shape of the μV/A profile to be examined. Dyck (*11*) showed that the shape can be used to infer information about the conductor orientation and discussed the complex variety of effects that conductors near the borehole can have on the data. Depending on the orientation of the conductor with respect to the borehole, various time channels can exhibit reversals of sign, as happened with the earliest channel, or maxima or minima. The inability to record data below the fracture (to avoid damaging the probe) limited the ability to interpret these results, since much of the diagnostic shape of the μV/A profile was lacking.

Figure 15 indicates that brine has affected the response up to a depth of nearly 100 m, although the strongest response is confined to the region near the fracture zone below 120 m. This fracture zone, not detected before injection, became very responsive during injection.

Figure 16 shows the contoured resistivities before and during injection, calculated from the Z component of the field after applying a ramp correction. The horizontal components were not used in those calculations, but are in data tables available from Tweeton. The resistivity sections were plotted as a function of time following transmitter current turnoff and receiver depth in borehole H14. Trends in the preinjection and injection data are generally similar except for somewhat lower resistivities in the injection data during early times, up to 0.25 ms, possibly due to brine saturating the zone around the borehole. Times are shown only to 1.6 ms because later times are of limited interest in this experiment.

The effects of noise are apparent as narrow zones of contrasting resistivity after 1 ms. Although this noise interferes with interpretation, it appears that injection caused a zone of low resistivity near 123 m depth. At this point the late-time (0.8 to 1.6 ms) resistivity has changed from greater than 125 Ω•m before injection to less than 75 Ω•m during injection. This depth correlates well with the major fracture at a depth of 120 m that carried brine from injection borehole H4 to borehole H14.

CONTROLLED-SOURCE AUDIOFREQUENCY MAGNETOTELLURICS

Of the two receiver configurations, only the less commonly used E_y/H_x (see figure 7) data showed a decrease in resistivity. The E_y/H_x preinjection, one-well injection,

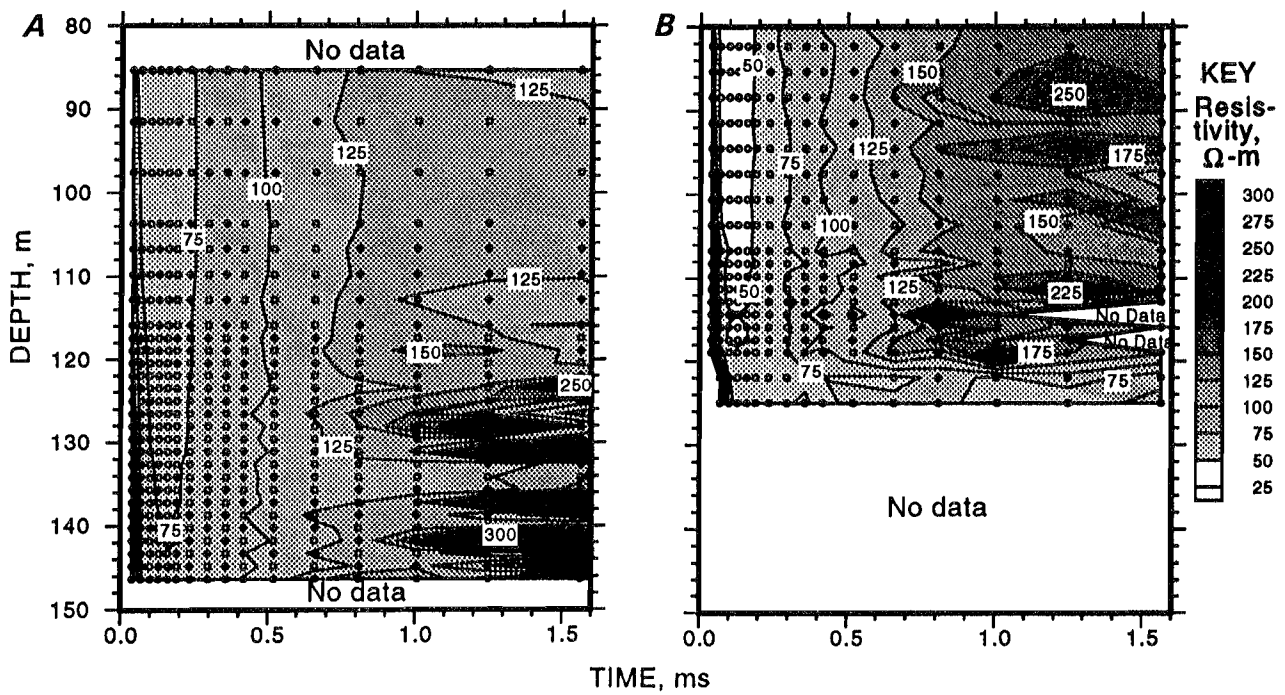

Figure 16.—Surface-borehole TEM contoured resistivities from borehole H14. *A*, Preinjection; *B*, one-well injection.

and two-well injection static-corrected resistivity sections using the Niblett-Bostick calculated depth, and the change from preinjection to two-well injection are shown in figure 17. Corresponding results for the E_x/H_y configuration are shown in figure 18.

While both preinjection data sets portray resistivity values characteristic of the area, the E_x/H_y data indicate values approximately 1.5 times higher than the E_y/H_x data. This "resistivity anisotropy" may be caused by the orientation of predominant fracture patterns, dipping geology, other unknown geologic features, static shift, or a combination of these factors.

The effect of the brine was different for the two injection data sets. The E_y/H_x results show the low-resistivity region that developed with injection is consistent with the anticipated location of the brine. The effect of south-dipping lithology and jointing appears in the E_y/H_x data set, especially near injection borehole H4. When compared with the preinjection data, brine appears to have moved toward the south, lowering the resistivity between H4, near station 90, and the end of the survey line at station 30. The lowest resistivity occurs at the expected depth of between 100 and 150 m.

Unlike the E_y/H_x data, the E_x/H_y data did not indicate the presence of the brine. A possible reason for this discrepancy is the difference in the orientation of brine-filled joints with respect to each of the configurations. It may be postulated that the E_y/H_x configuration was more sensitive to the predominant direction of the brine-induced electric and magnetic fields. The E_y field, in particular, may have been oriented roughly perpendicular to the developing plume, increasing its response. The field direction with the highest magnitude will be detected most easily and will give the clearest indication of the conductive plume. The results demonstrate the desirability of measuring both sets of fields when monitoring with CSAMT.

While the implied direction of flow seems reasonable, the location of accumulated brine is not clearly defined by the E_y/H_x resistivity. A general lowering of resistivity occurs during injection near borehole H4 and the water table, but no isolated response is observed. Clearly, the averaging effects of the overlying layers are masking a portion of the signal.

The preinjection, one-well injection, and two-well injection E_y/H_x phase differences are shown in figure 19. For E_y/H_x preinjection data, there is little deviation from the nominal 785 mrad value from near surface to a depth of about 80 m, indicating unchanging resistivity. Below 80 m, corresponding to a frequency of 1,024 Hz, the phase difference increases, which indicates the presence of a conductive layer. The conductive layer probably corresponds to the capillary fringe above the water table. At greater depths, a strong phase reversal, trending toward negative values, occurs, beginning at 512 Hz.

The corresponding E_x/H_y phase differences are shown in figure 20. For comparison, the E_y/H_x phase differences for the lowest three frequencies increased significantly with injection, going from about 0 to about 200 mrad. The E_x/H_y phase differences changed much less, confirming less effect from the brine for this receiver configuration.

The very small E_x/H_y phase differences near the 160-m station strongly affected the calculated resistivities. (The small phase differences may have been caused by a power-line.) The E_x/H_y resistivity, corrected for static effects using the phase differences, was very large at the 160-m station. This feature was caused by the static correction calculation because there wasn't a corresponding feature in the E_x or H_y data.

Calculations were made to determine if static corrections could be avoided by using only the change in uncorrected resistivity with injection. The important factor in monitoring is the change in resistivity. If the change with injection for the uncorrected resistivity was similar to the change for the corrected resistivity, then the calculations could be simplified by avoiding the static corrections. Pseudosections of the uncorrected resistivities were generated and the changes with injection were calculated. However, the changes in the uncorrected resistivities were so erratic that no meaningful interpretation could be made. These results indicate the importance of the static corrections to CSAMT.

SURFACE-BOREHOLE FREQUENCY-DOMAIN ELECTROMAGNETIC METHOD

Profiles for three frequencies of the Z-component normalized magnetic induction data from borehole H14 are displayed in figure 21. The preinjection profiles show smooth gradients, decreasing in amplitude from surface to depth, as would be expected from the gradually weakening signal of the surface transmitter as the probe is lowered. The injection data, however, show high variability in magnitude due to brine-saturated fractures.

The injection data demonstrate that the peak response magnitude can increase by as much as a factor of 5, depending on frequency. The observation that intermediate frequencies gave the greatest response suggests that measurements should be made over a suite of frequencies in the audio range. The individual peaks roughly correspond to peaks observed in a preinjection Geonics EM-39 induction log (figure 22) in borehole H14, supporting a fracture interpretation. (The injection log is not shown.)

To minimize damage to the receiver probe from submerging it in salt water, most of the injection data were recorded immediately after termination of injection, allowing large concentrations of salt water to drain. The data show that enough residual brine remained to enhance the fracture conductivity, observable as large peaks. The largest peak, located at a depth between 122 and 125 m, is probably an indication of residual brine in the known fracture zone near 120 m.

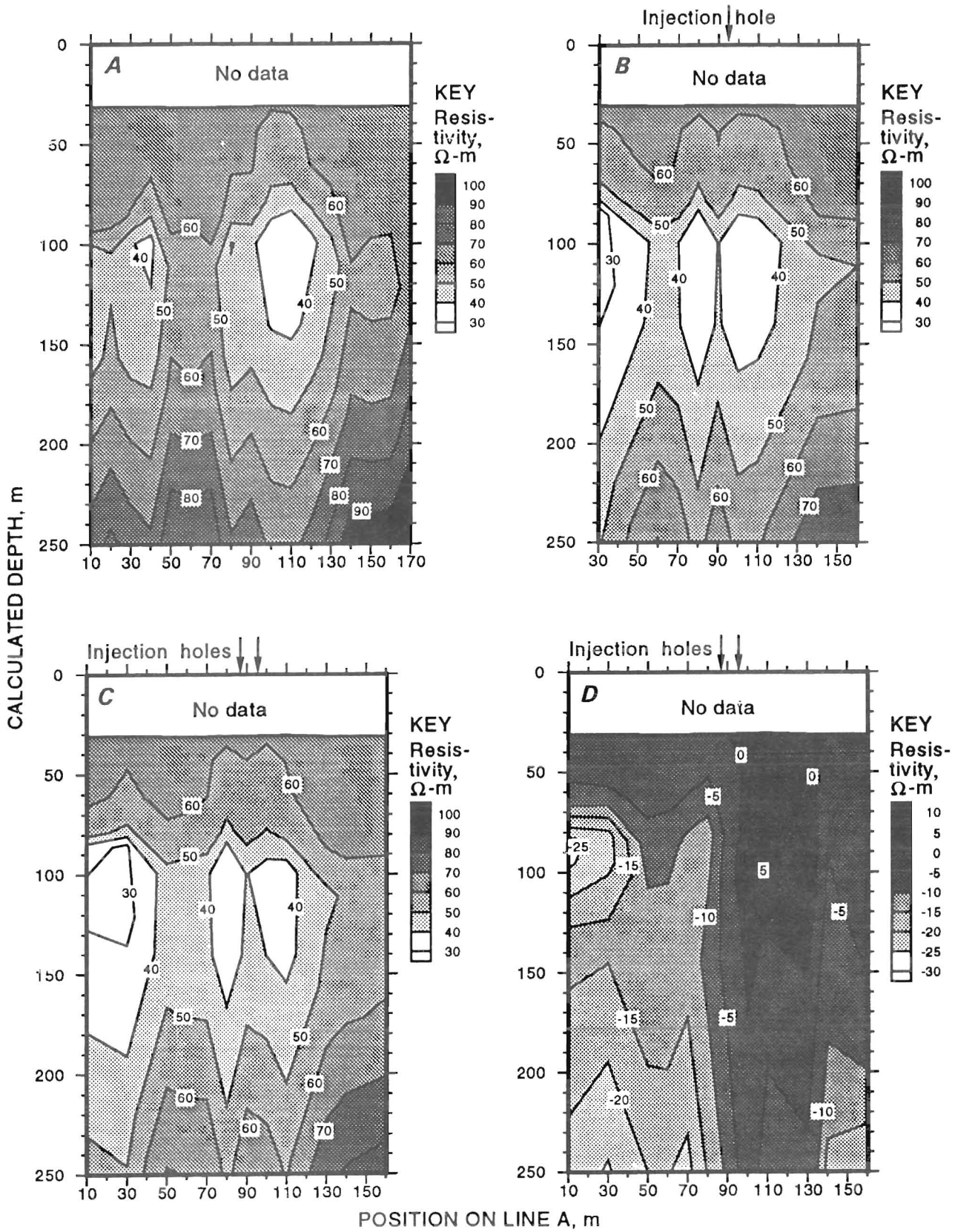

Figure 17.—CSAMT E_y/H_x resistivity pseudosections, line A. *A*, Preinjection; *B*, one-well injection; *C*, two-well injection; *D*, two-well injection minus preinjection.

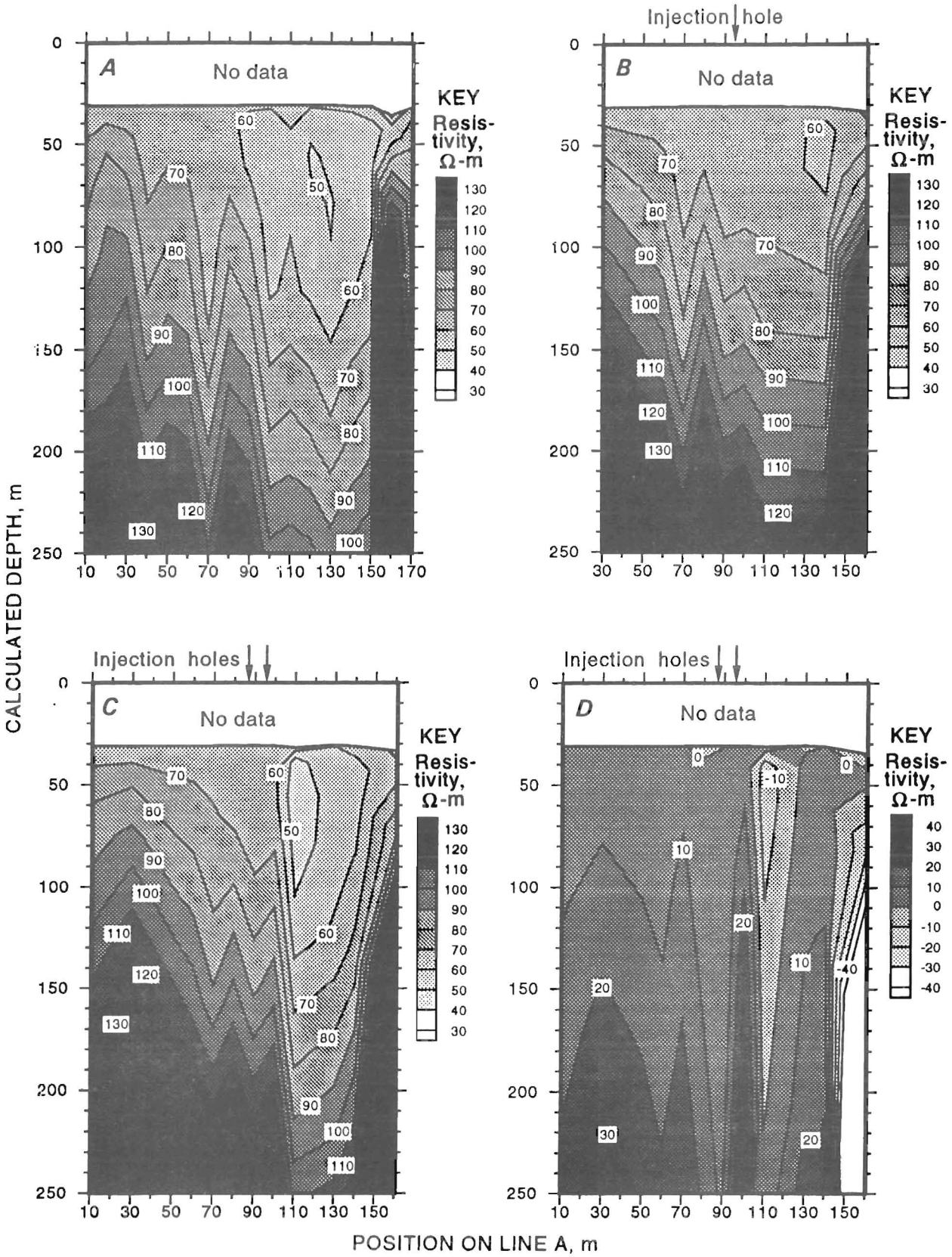

Figure 18.—CSAMT E_x/H_y resistivity pseudosections, line A. *A*, Preinjection; *B*, one-well injection; *C*, two-well injection; *D*, two-well injection minus preinjection.

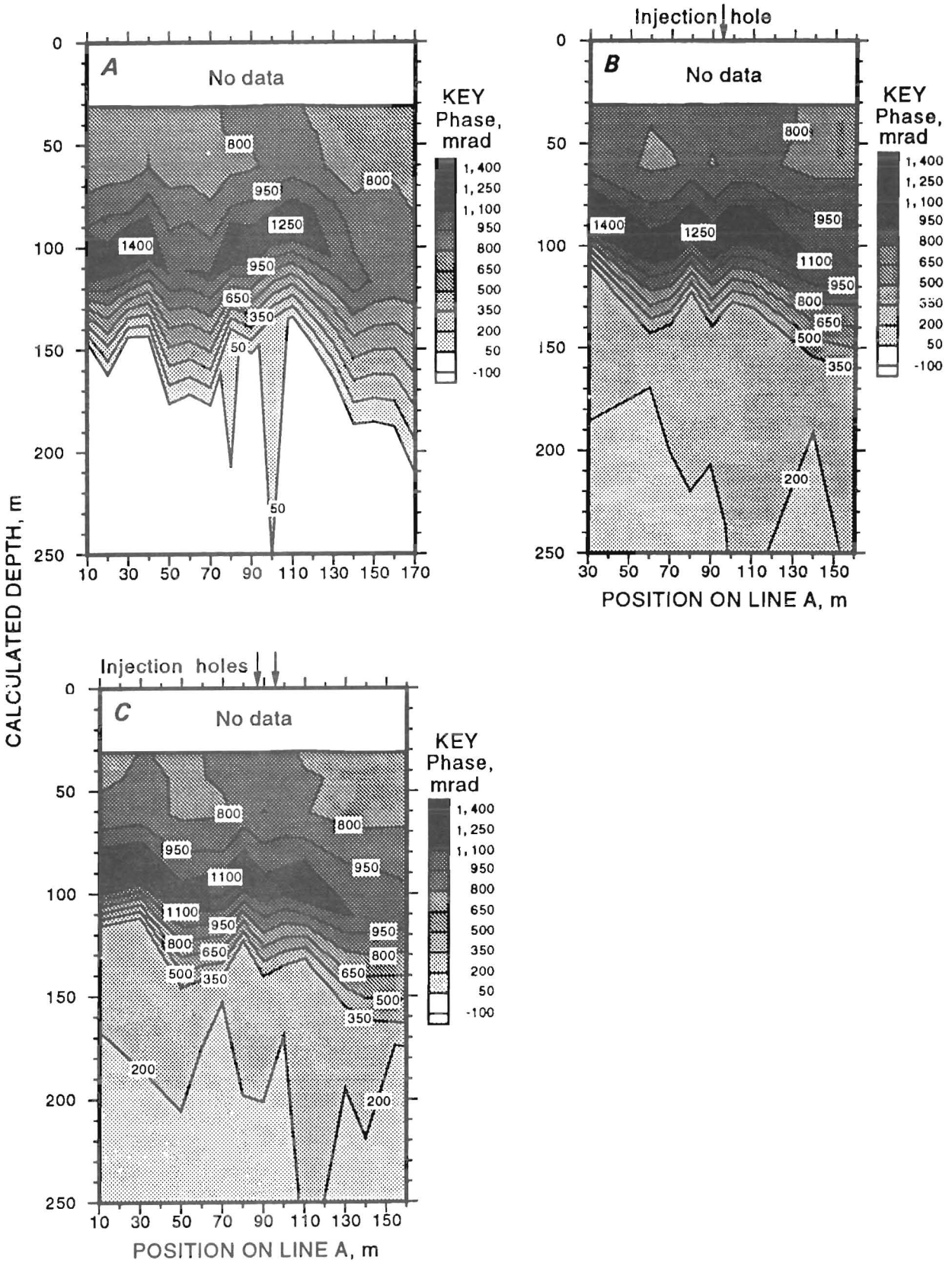

Figure 19.—CSAMT E_y/H_x phase difference pseudosections, line A. *A*, Preinjection; *B*, one-well injection; *C*, two-well injection.

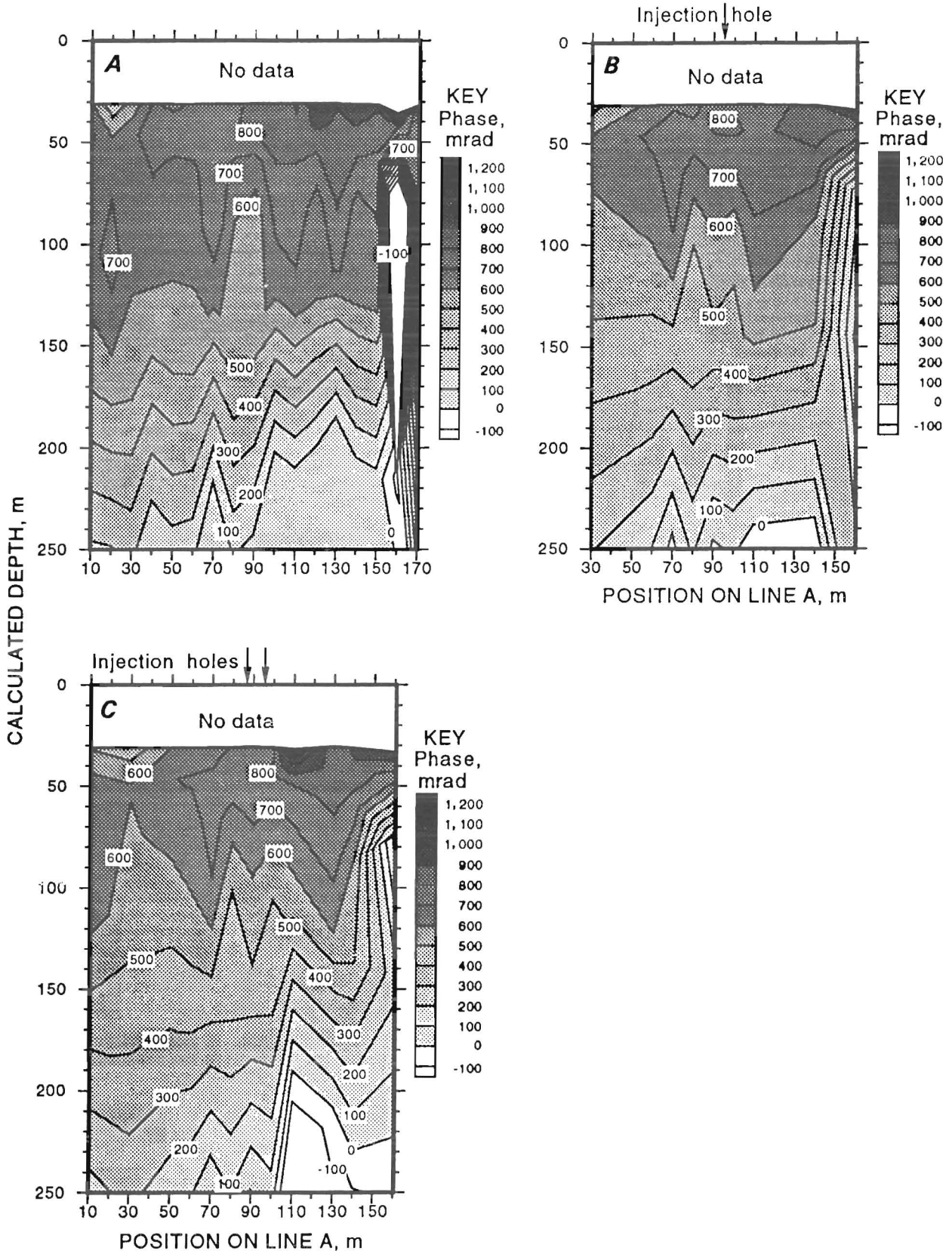

Figure 20.—CSAMT E_x/H_y phase difference pseudosections, line A. *A*, Preinjection; *B*, one-well injection; *C*, two-well injection.

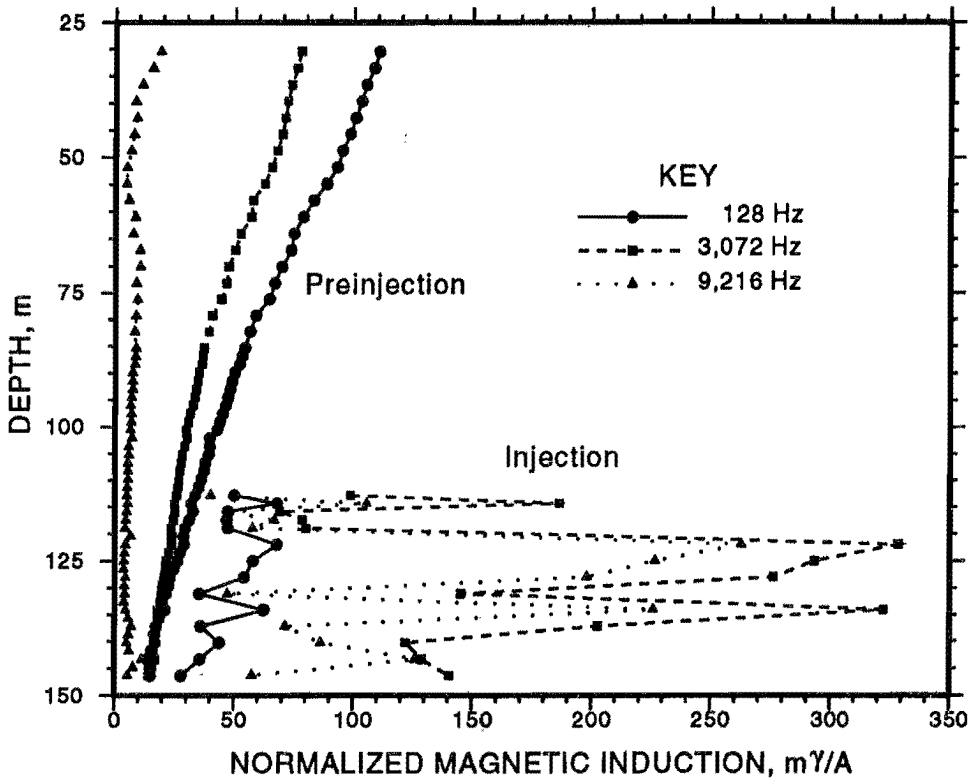

Figure 21.—Surface-borehole FEM Z component of normalized magnetic inductions in borehole H14.

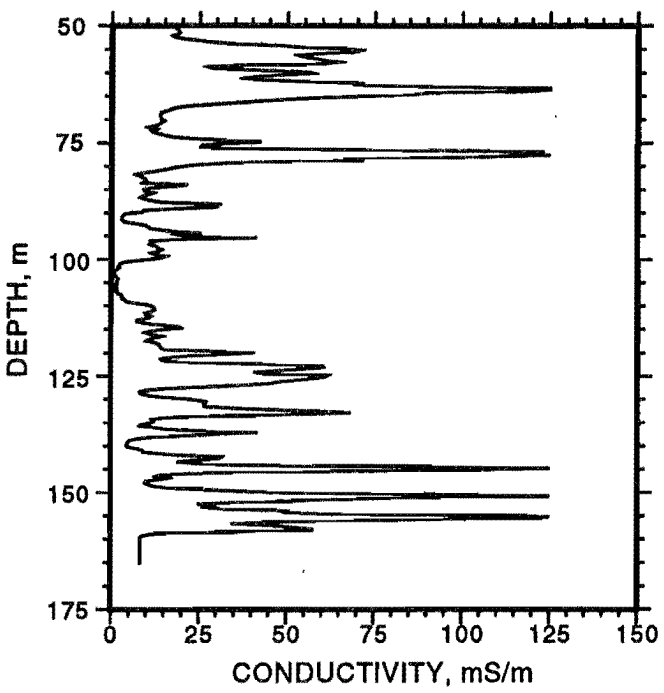

Figure 22.—Preinjection induction log in borehole H14.

The effectiveness of the surface-borehole FEM method was verified by injecting brine while taking measurements at a depth of 91 m in borehole H15. Results are shown in figure 23. This depth was chosen to show the probe's sensitivity to the brine at a distance sufficient to test the method conclusively. The receiver was an estimated 35 to 40 m from the injection point (the bottom of H4), and over 60 m above the water table, where the brine would collect. An increase in the magnetic induction, especially in the higher frequencies, occurred 20 min after the start of injection. The response time of 20 min at 30 L/min indicates that the system detected only 600 L of brine, a minimum of 35 m from the receiver. This result shows promise for the system to serve as a monitoring supplement to examine the region between boreholes.

The horizontal components were used to obtain a horizontal ellipticity value. Preinjection and injection ellipticity data at seven selected frequencies are illustrated for a portion of borehole H14 in figure 24. The preinjection data set is relatively flat at low frequencies but becomes increasingly more responsive at high frequencies. This may be a reflection of small conductivity changes associated with clay-filled fractures. The large fracture zone near 120 m may be indicated as a negative-to-positive swing, but

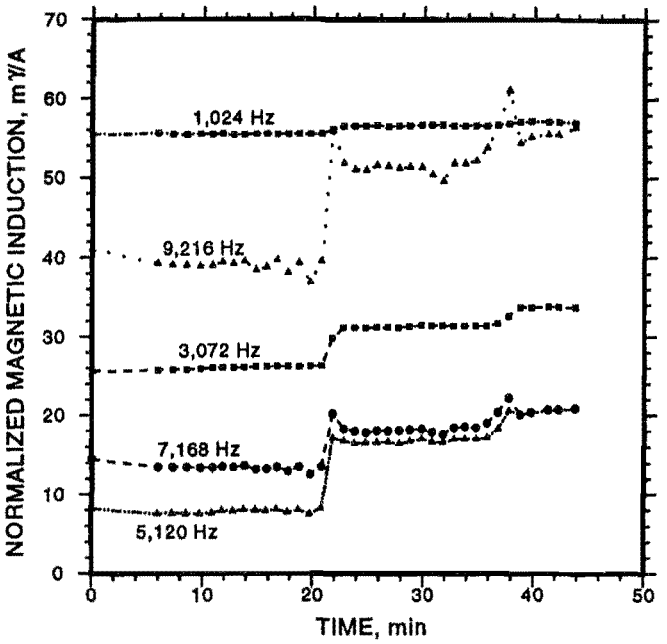

Figure 23.—Surface-borehole FEM Z component of normalized magnetic induction in injection borehole H15 as function of time during injection.

this is not certain. The highest frequency may have been attenuated by the presence of residual clays or conductive mineralization in the fracture.

The injection data set is significantly different from the preinjection set, particularly in the vicinity of the fracture zone near 120 m. The low-frequency data illustrate a pronounced effect from the brine, which was probably slowly draining from the fracture during the measurements. As the frequency is increased, the attenuating effect of the brine becomes more apparent, until at very high frequencies, there is almost no indication of the fracture zone. An alternative interpretation may include a breakdown of response linearity as the conductivity or frequency becomes very high.

Other responses occur at depths somewhat shallower than 120 m, although the fluid was not known to rise above the 120-m level during injection. Small amounts of brine may have flowed through the perforated casing at many depths as the brine moved down the borehole wall.

The injection data show a sign reversal between 640 and 896 Hz at a depth of about 118 m. This may be a result of the "skin effect," or the differential penetration of high- and low-frequency currents into different portions of the conductive brine. At frequencies above 1,024 Hz, the profiles tend to smooth because of the attenuating effect of the highly conductive fluid. For in situ mining applications, these frequency-dependent changes in conductivity may help identify fractures having a high flow capacity. The sharp spatial-dependent changes indicate that small station spacings are required for effective fluid mapping.

CROSSHOLE FREQUENCY-DOMAIN ELECTROMAGNETIC METHOD

Most of the data were collected while the transmitter was kept at 125 m depth in injection borehole H15 and the receiver depth in borehole H14 was varied from 116 to 146 m before and during injection. Normalized magnetic inductions for three frequencies from each set of data are shown in figure 25. All three components of the magnetic field were recorded, but only the vertical component will be discussed here.

The preinjection data are generally featureless except for a broad low-amplitude peak centered near a depth of 128 m. This peak may be due to the increased field strength near the transmitter probe, at a depth of 125 m in the adjacent borehole.

The injection magnetic inductions are much larger than the preinjection data. This effect may have been caused by brine filling the annulus around the casing. A peak in the data near 120 m correlates with a known fracture at that depth. Other peaks at depths of 131, 137, and 143 m correlate with fractures or fracture zones inferred from the EM-39 induction log (figure 22). Local peaks in the profiles suggest that brine has infiltrated fracture zones at depths of 118, 131, 137, and 143 m. However, the wide station spacing hindered detailed interpretation.

As in the surface-borehole FEM survey, the effectiveness of the crosshole method was tested by measuring response as a function of time after the start of injection. For this part of the test, the transmitter was held at a depth of 130 m in injection borehole H15 while the receiver was alternated between depths of 114 and 116 m in borehole H14. The results are shown in figure 26. After about 60 min of injection, a change in response was observed at 116 m, increasing from 50 to over 70 mγ. Further changes did not occur even after injection was stopped at 63 min and restarted at 80 min, suggesting that nearby fractures retained brine for that time. At a receiver depth of 114 m, variations in the data appeared to correlate with the starting, stopping, and restarting of injection, although the changes were much smaller than those observed at a depth of 116 m. These variations suggest increased sensitivity to the low-retention capacity of fractures near this level. In any case, the crosshole system was reacting to the influx of brine and appears useful for locating saturated fractures.

SURFACE MAGNETIC FIELD ELLIPTICITY

Figure 27 shows the apparent-resistivity pseudosections and the injection value minus the preinjection value for each point. A substantial decrease in apparent resistivity at depth is indicated by the negative differences near the

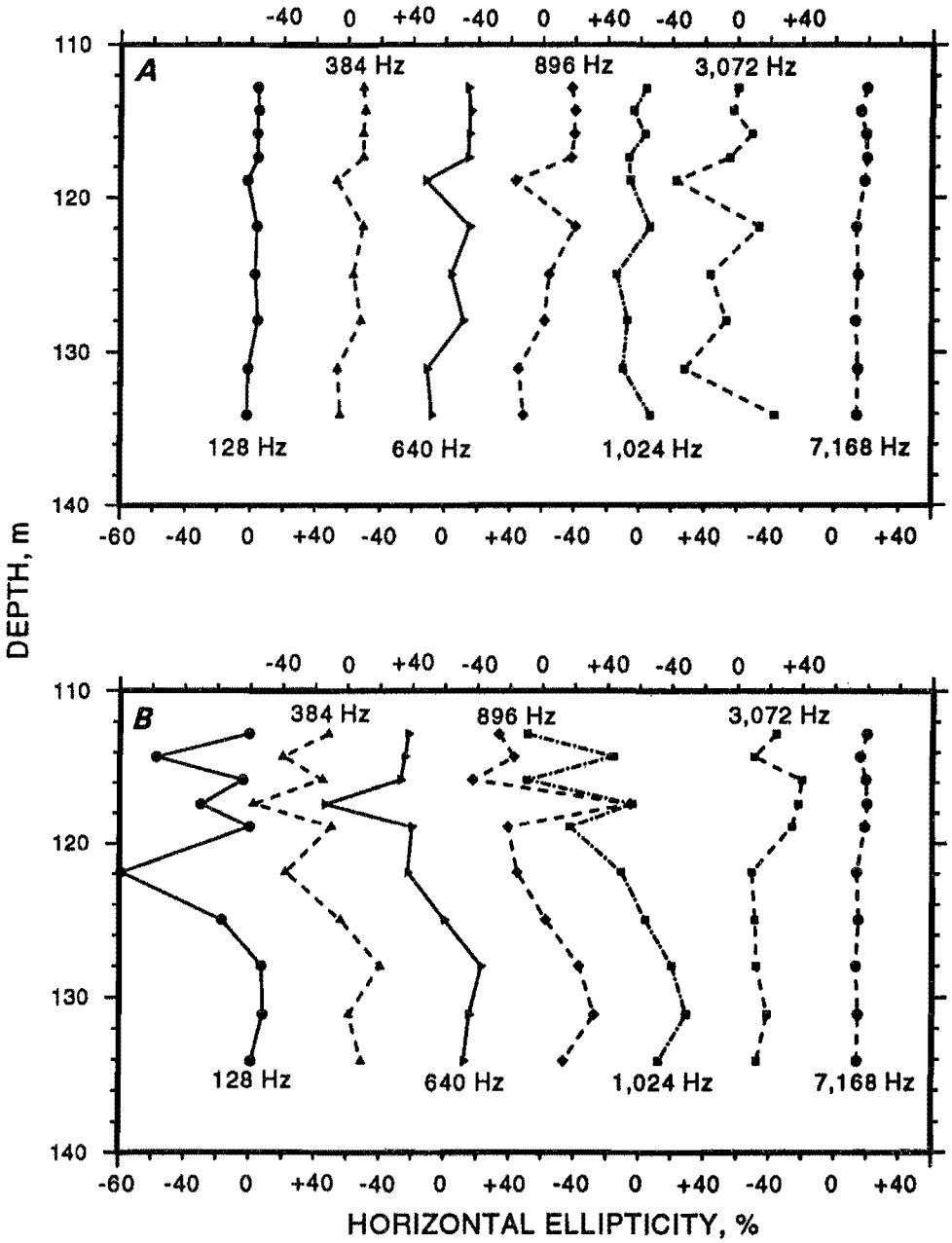

Figure 24.—Surface-borehole FEM ellipticities in borehole H14. *A*, Preinjection; *B*, one-well injection. The % ellipticity axis has a segment for each frequency, with the zero point for each segment close to the corresponding frequency label.

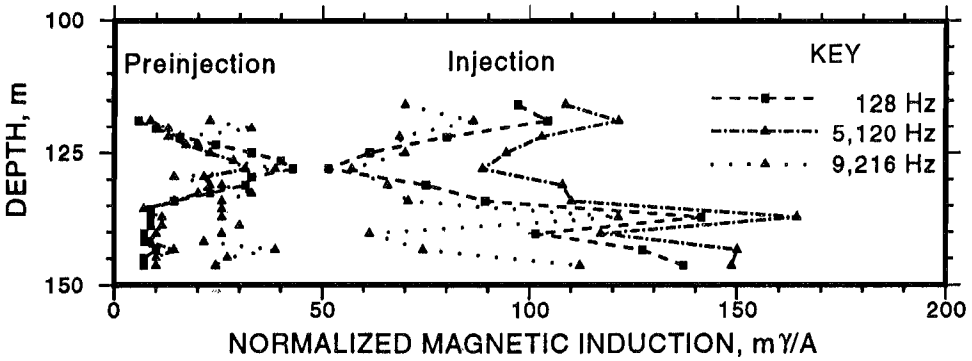

Figure 25.—Crosshole FEM Z component of normalized magnetic inductions. Transmitter in injection borehole H15 at 125 m. Receiver in borehole H14 at indicated depths.

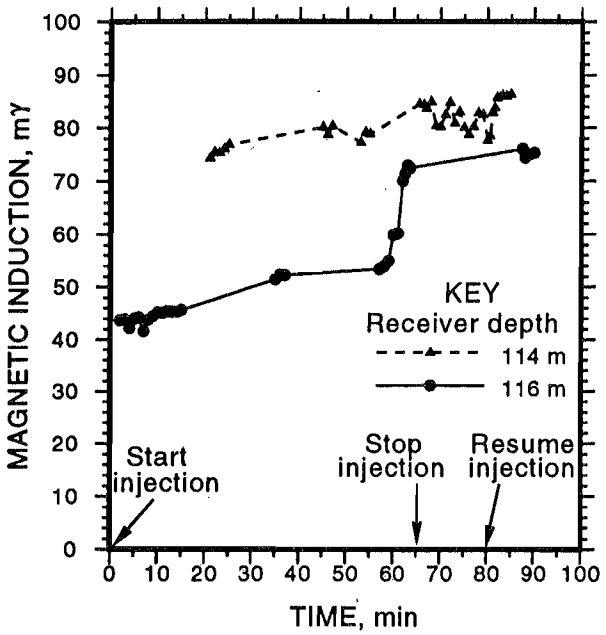

Figure 26.—Crosshole FEM Z component of normalized magnetic induction as function of time during injection. Transmitter in injection bore-hole H15 at 130 m. Receiver in borehole H14 at 114 and 116 m. Frequency = 1,024 Hz.

bottom of figure 27*C*. This change is attributed to the brine spreading at the water table, at 157 m depth.

The increase in apparent resistivity to the right of injection borehole H4 is probably related to the powerline directly over this anomaly. The powerline was disconnected and grounds were removed during all the measurements. It was reconnected and the grounds replaced between measurements. There was probably a small change in the impedance to ground of the powerline wires in the preinjection versus injection surveys that led to the anomalous response under the powerlines.

The pseudosections shown in figure 27 do not necessarily provide a geometrically accurate section. Further modeling and inversion of the data are needed to determine the precise depths and character of the resistivity structure. Unfortunately, such modeling is severely limited using state-of-the-art modeling programs since the powerline was 2-D and the plume of brine was 3-D.

Differences between the layering observed with this system and the other surface methods may be at least partially caused by the difference in inversion methods. The ellipticity data were not inverted with the Niblett-Bostick inversion. The depth was estimated using a normalized skin-depth scale that was determined by comparison with 1-D models, whereas the TEM and CSAMT depths were calculated as part of the inversion process. Thus, exact correspondence in layering should not be expected. An additional difference is that the ellipticity system used more frequencies than the CSAMT system. Therefore, features that would cause a response at a particular frequency may not be observed with a CSAMT system lacking that frequency. For example, the ellipticity system provides higher frequencies and therefore can display features closer to the surface.

The ellipticity method offers several advantages compared with the other surface methods. The many closely-spaced frequencies over a broad range are helpful for profiling thin features that can be either shallow or deep. Unlike CSAMT, the ellipticity method does not need electric dipoles, so it avoids static effects, and it does not need a distant transmitter. It appeared to be less susceptible to electrical noise and interference from surface conductors than the TEM method. However, both the ellipticity method and CSAMT were affected by the powerline near the north (high station number) end of the survey line.

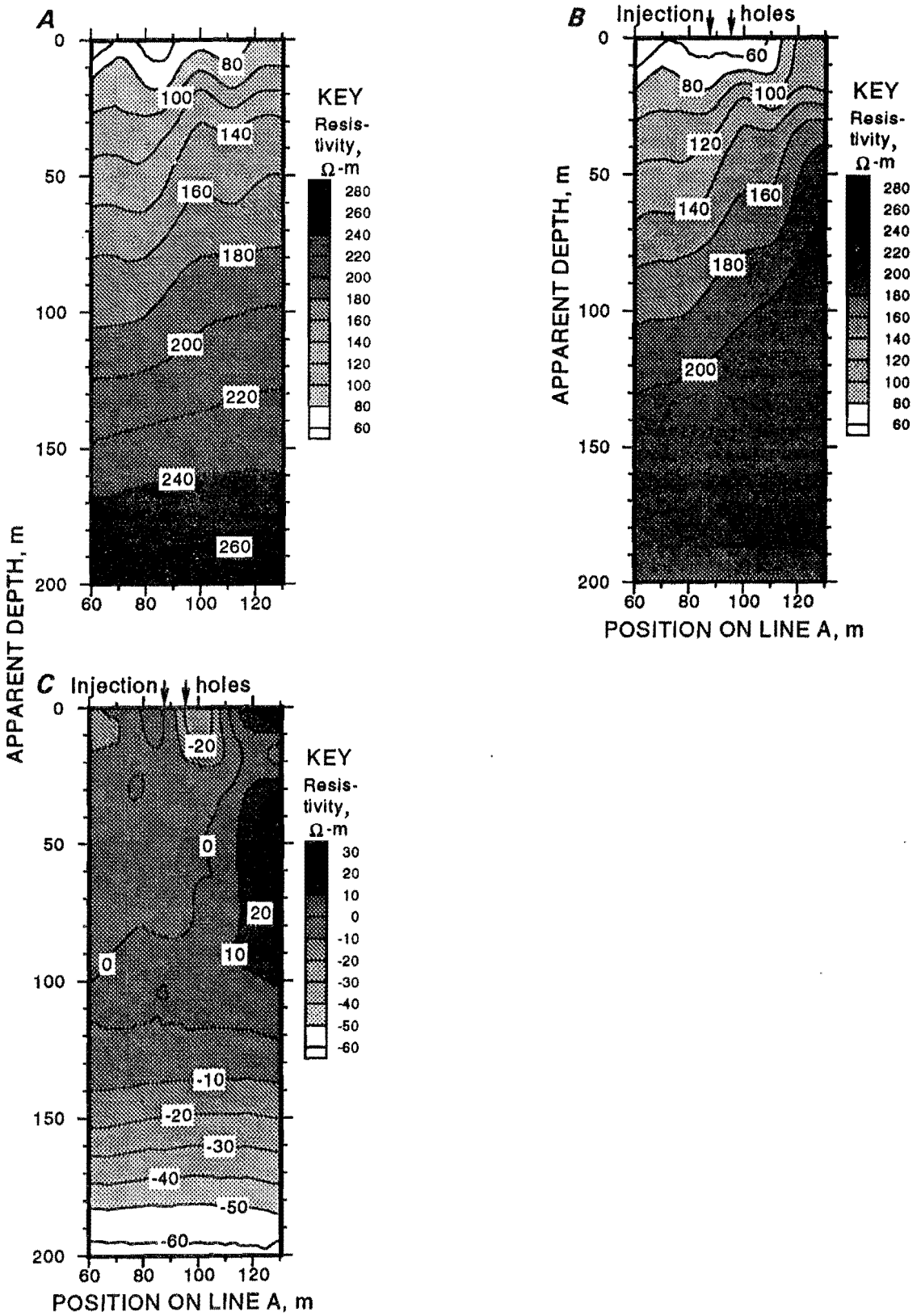

Figure 27.–Surface magnetic field ellipticity, resistivity pseudosections along line A. *A*, Preinjection; *B*, two-well injection; *C*, two-well injection minus preinjection.

CONCLUSIONS

Selected EM geophysical systems were evaluated for their ability to detect injected salt water brine with a conductivity of 3.6 S/m collecting at the water table, 157 m subsurface. A total of 110,000 L of brine was injected. The effective target volume was probably much less than that at any time during the test.

Despite the small target and deep water table, the surface TEM, CSAMT, and magnetic field ellipticity methods showed decreases in resistivity with injection consistent with a response to the brine. In addition, surface-borehole and crosshole methods detected fractures containing brine. Each system revealed particular advantages and disadvantages.

The surface TEM results showed a broad decrease in resistivity with injection, along with an interfering narrow response from a surface metallic conductor. The surface TEM method was logistically convenient because it did not require grounded electric dipoles, but it appeared more susceptible than the frequency-domain systems to electrical noise and the effects of a surface metallic conductor. TEM data were strongly affected by a surface metallic conductor that appeared as a deep feature in a resistivity pseudosection because it produced a long time constant. Surface-borehole TEM data indicated strong changes as a result of brine injection and located brine-filled fractures. The CSAMT survey revealed resistivity changes using E_y/H_x measurements, but not with the more commonly used E_x/H_y data. This result may have been due to differences in EM coupling with fracture-controlled brine flow. Data collection was slower with CSAMT than with the TEM method because data collection with CSAMT required grounded electric dipoles. However, CSAMT data were less affected by the surface metallic conductor. Static effects were large enough that failing to apply proper corrections would lead to the wrong interpretations.

A discrepancy between the CSAMT and TEM methods in the determination of apparent depth to the brine may be caused by inaccurate (1-D) TEM inversion or weak EM coupling due to transmitter-target-receiver geometry.

Surface-borehole FEM tests showed high sensitivity to the brine, indicating promise for monitoring applications. While time-dependent changes due to injection were measured, surface-borehole FEM tests detected 600 L of brine with the receiver at a depth of 91 m, over 35 m from the injection point and over 60 m above the water table. It also located conductive zones consistent with an EM induction log, interpreted to be zones of fracturing. Responses may vary with frequency in a complex way, depending on fracture geometry and conductivity, so a suite of frequencies should be employed. In addition, a novel approach using the two horizontal components to compute ellipticity was very responsive to brine injection.

The crosshole FEM method provided data consistent with a conductivity log, insofar as comparisons could be made. Conductive zones generally appeared as peaks at correct locations, but the data set may be somewhat distorted by changes in the primary field strength as the distance varied between the fixed transmitter and the mobile receiver. However, changes in the data with brine injection were easily recognizable. The horizontal resolution and sensitivity of the method are not known at this time. Data recorded at many transmitter and receiver sites would provide greater interrogation of the region between boreholes and may allow tomographic image processing, improving both horizontal and vertical resolution.

The surface magnetic field ellipticity surveys indicated a decrease in resistivity at depth following brine injection, which is consistent with brine at and below the water table, affecting surface readings over much of the survey line. This method offers the advantage of a frequency-domain system's reduced susceptibility to electrical noise. Unlike CSAMT, however, the ellipticity method avoids electric dipoles and the resulting static effects and does not require a distant transmitter.

Surface ellipticity and CSAMT methods were both affected by an anomalous interference near the north (high station number) end of the survey line. CSAMT data showed a large anomalous change in phase difference and a change in the resistivity calculated using phase differences to make static corrections. Ellipticity data showed a large increase in resistivity there, whereas the brine would have produced a decrease.

Measuring all the components of electric and magnetic fields available with selected methods was beneficial. TEM horizontal magnetic components helped to identify the source of interference with the usual vertical component data. FEM surface-borehole horizontal magnetic components allowed surface-borehole ellipticity to be calculated. With CSAMT, only the less commonly measured fields showed a response to the brine. When using a selected method, measuring all the available components of the fields will be especially important for monitoring in complex geology and fractured rock, where resistivity anisotropy is likely.

Monitoring conductive solutions presents a different set of challenges than exploration. The effect will often be more subtle, and the target will usually be smaller. Collecting data before and after injection is important for detecting small changes in resistivity. Geology can be complex, especially near mines, and monitoring requires separating the large effects of geology from the subtle effects of the solution. Future needs include more 3-D interpretation because monitoring is a 3-D problem.

The data collected in this test did not allow the brine position to be located with the accuracy needed for determining the flow pattern in a well field. The results suggested possible improvements in conducting future tests. Additional data collection could have enhanced the test. Longer survey lines, with the half-length greater than the depth to the water table, would have allowed a better test of lateral resolution. Additional parallel survey lines would have allowed 3-D effects to be examined. A waterproof probe would have allowed more complete downhole data collection, and more boreholes extending to the water table could have provided independent verification of the position of the brine.

Detecting the small amount of brine at the depth of this experiment was a significant achievement for these systems. The results demonstrated considerable promise for expanding the role of EM methods in detecting and monitoring subsurface conductive solutions.

REFERENCES

1. Ahlness, J. K., D. R. Tweeton, W. C. Larson, D. J. Millenacker, and R. D. Schmidt. In Situ Mining of Hard-Rock Ores. Sec. in SME Mining Engineering Handbook, ed. by H. L. Hartman. Soc. Min. Met. and Expl. Inc., 2d ed., 1992, pp. 1515-1528.

2. Anderson, W. L. Iterative Inversion of Dipole Loop-Loop Electromagnetic Data for Layered Earth Models Using Numerical Integration and Complex Image Theory. U.S. Geol. Surv. OFR 92-553-A (printed) and 92-553-B (diskette), 1992, 42 pp.

3. Bak, N. H., B. K. Sternberg, S. L. Dvorak, and S. J. Thomas. Rapid, High-Accuracy Electromagnetic Soundings Using a Novel Four-Axis Coil To Measure Magnetic Field Ellipticity. J. Appl. Geophys., v. 30, 1993, pp. 235-245.

4. Bartel, L. C. Results From a Controlled-Source Audiofrequency Magnetotelluric Survey To Characterize an Aquifer. Ch. in Investigations in Geophysics, No. 5, Geotechnical and Environmental Geophysics, Vol. II: Environmental and Groundwater, ed. by S. H. Ward. Soc. Explor. Geophys., Tulsa, OK, 1990, pp. 219-233.

5. Beck, A. E. Physical Principles of Exploration Methods. Wiley, New York, 1981, 234 pp.

6. Bevc, D., and H. F. Morrison. Borehole-to-Surface Electrical Resistivity Monitoring of a Salt Water Injection Experiment. Paper in 1989 Technical Program. Expanded Abstracts With Biographies (59th Annu. Int. Meet., Dallas, TX, Oct. 29-Nov. 2, 1989). Soc. Explor. Geophys., 1989, pp. 216-218.

7. Bostick, F. X., Jr. Electromagnetic Array Profiling (EMAP). Paper in 1986 Technical Program. Expanded Abstracts With Biographies (56th Annu. Int. Meet., Houston, TX, Nov. 2-6, 1986). Soc. Explor. Geophys., 1986, pp. 60-61.

8. ____. A Simple Almost Exact Method of MT Analysis. Paper in Proceedings of the University of Utah Workshop on Electrical Methods in Geothermal Exploration. Univ. UT, Salt Lake City, UT, 1977, pp. 175-188.

9. Cagniard, L. Basic Theory of the Magnetotelluric Method of Geophysical Prospecting. Geophysics, v. 18, 1953, pp. 605-635.

10. Chemical Rubber Publishing Co. CRC Handbook of Chemistry and Physics. CRC Press, Boca Raton, FL, 1979, p. D-271.

11. Dyck, A. V. Drill-Hole Electromagnetic Methods. Ch. 11 in Electromagnetic Methods in Applied Geophysics, v. 2, Application, Part B, Investigations in Geophysics, No. 3, ed. by M. N. Nabighian. Soc. Explor. Geophys., 1991, pp. 881-930.

12. Fitterman, D. V., and W. L. Anderson. Effect of Transmitter Turn-Off Time on Transient Soundings. Geoexploration, v. 24, No. 2, 1987, pp. 131-146.

13. Fitterman, D. V., and M. T. Stewart. Transient Electromagnetic Sounding for Groundwater. Geophysics, v. 51, No. 4, 1986, pp. 995-1005.

14. Frischknecht, F. C., V. F. Labson, B. R. Spies, and W. L. Anderson. Profiling Methods Using Small Sources. Ch. 3 in Electromagnetic Methods in Applied Geophysics, v. 2, Application, ed. by M. N. Nabighian. Soc. Explor. Geophys., 1991, pp. 168-174.

15. Greenhouse, J. P., and D. D. Slaine. The Use of Reconnaissance Electromagnetic Methods To Map Contaminant Migration. Ground Water Monit. Rev., v. 3, No. 2, 1983, pp. 47-59.

16. Hanson, J. C. Applicability of Electrical Methods in Deep Detection and Monitoring of Conductive Lixiviants. BuMines IC 9308, 1992, 31 pp.

17. Hanson, J. C., D. R. Tweeton, and M. J. Friedel. A Geophysical Field Experiment for Detecting and Monitoring Conductive Fluids. Leading Edge, v. 12, No. 9, Sept. 1993, pp. 930-937.

18. Hanson, J. C., D. R. Tweeton, M. J. Friedel, and L. J. Dahl. A Field Test of Electromagnetic Methods for the Detection of Conductive Plumes. Paper in 1991 Technical Program. Expanded Abstracts With Biographies (61st Annu. Int. Meet., Houston, TX, Nov. 10-14, 1991). Soc. Explor. Geophys., 1991, pp. 569-572.

19. Heidrick, T. L., and S. R. Titley. Fracture and Dike Patterns in Laramide Plutons and Their Structural and Tectonic Implications. Ch. in Advances in Geology of the Porphyry Copper Deposits, Southwestern North America, ed. by S. R. Titley. Univ. AZ Press, 1982, pp. 73-91.

20. Hoekstra, P., C. H. Stoyer, B. A. James, and M. W. Blohm. Characterization of Reservoir Rocks and Fluids by Surface Electromagnetic Transient Methods. Dep. Energy, Bartlesville, OK, DOE contract DE-AC22-90BC14476, 1992, 61 pp.

21. Hoversten, G. Comparison of Time and Frequency Domain EM Sounding Techniques. Ph.D. Dissertation, Univ. CA, Berkeley, CA, 1981, 170 pp.

22. Jones, A. G. On the Equivalence of the "Niblett" and "Bostick" Transformations in the MT Method. J. Geophys., v. 53, 1983, pp. 72-73.

23. Lee, D. O., and J. R. Wayland. Electromagnetic Geophysical Leaching Plume Detection Experiment—San Xavier Mine Facility, Tucson, Arizona. Sandia Nat. Lab. Rep. SAND91-0191, 1991, 31 pp.

24. McNeill, J. D. Advances in Electromagnetic Methods for Groundwater Studies. Paper in Proceedings of the Symposium on the Application of Geophysics to Engineering and Environmental Problems (SAGEEP). CO Sch. Mines, Golden, CO, 1988, pp. 251-348.

25. ____. Electromagnetic Terrain Conductivity Measurement at Low Induction Numbers. Geonics, Ltd., Ontario, Canada, TN-6, Oct. 1980, 15 pp.

26. Mills, T., P. Hoekstra, M. Blohm, and L. Evans. The Use of Time Domain Electromagnetic Soundings for Mapping Sea Water Intrusion in Monterey County, CA: A Case History. Ground Water, v. 26, No. 6, Nov.-Dec. 1988, pp. 771-782.

27. Nabighian, M. N., and J. C. Macnae. Time Domain Electromagnetic Prospecting Methods. Ch. 6 in Electromagnetic Methods in Applied Geophysics, v. 2, Application, ed. by M. N. Nabighian. Soc. Explor. Geophys., 1991, pp. 427-520.

28. Nelson, R. G., and J. H. Haigh. Geophysical Investigations of Sinkholes in Lateritic Terrains. Geotechnical and Environmental Geophysics, v. III, Geotechnical, No. 5 in Series Investigations in Geophysics. Soc. Explor. Geophys., 1990, pp. 133-153.

29. Niblett, E. R., and C. Sayn-Wittgenstein. Variation of Electrical Conductivity With Depth by the MT Method. Geophysics, v. 25, 1960, pp. 998-1008.

30. Petersen, R., J. Hild, and P. Hoekstra. Geophysical Studies for the Exploration of Ground Water in the Basin and Range of Northern Nevada. Paper in Proceedings of the Symposium on the Application of Geophysics to Engineering and Environmental Problems (SAGEEP). CO Sch. Mines, Golden, CO, 1989, pp. 425-435.

31. Ryu, J., F. Morrison, and S. Ward. Electromagnetic Depth Sounding Experiment Across Santa Clara Valley. Geophysics, v. 37, 1972, pp. 351-374.

32. Sandburg, S. K. Microcomputer Software for the Processing and Forward Modeling of Transient Electromagnetic Data Taken in the Central Loop Sounding Configuration. NJ Geol. Surv. Open-File Rep. 88-1, Trenton, NJ, 1988, 88 pp.

33. Sheriff, R. E. Encyclopedic Dictionary of Exploration Geophysics. Soc. Explor. Geophys., 1991, p. 271.

34. Smith, B. Interpretation of Electromagnetic Field Measurements. Ph.D. Thesis, Univ. UT, Salt Lake City, UT, 1975, 244 pp.

35. Spies, B. R., and D. E. Eggers. The Use and Misuse of Apparent Resistivity in Electromagnetic Methods. Geophysics, v. 51, No. 7, 1986, pp. 1462-1471.

36. Spies, B. R., and F. C. Frischknecht. Electromagnetic Sounding. Ch. in Electromagnetic Methods in Applied Geophysics, v. 2, Application, Part A, Investigations in Geophysics, No. 3, ed. by M. N. Nabighian. Soc. Explor. Geophys., 1991, pp. 363-374.

37. Sternberg, B. K. High-Resolution Electromagnetic (EM) Imaging of Subsurface Contaminant Plumes. Paper in Proceedings of Environmental Research Conference on Groundwater Quality and Waste Disposal (Washington, DC, May 2-4, 1989). U.S. Environ. Prot. Agency, EN-6749, 1990, pp. 18-1 to 18-26.

38. Sternberg, B. K., P. L. Buller, J. L. Kisabeth, and E. Mehreteab. Electrical Methods for Hydrocarbon Exploration II, Magnetotelluric (MT) Method. Paper in Unconventional Methods in Exploration for Petroleum and Natural Gas III, ed. by M. J. Davidson and B. M. Gottlieb. South. Methodist Univ. Press, 1984, pp. 202-230.

39. Sternberg, B. K., and R. Nopper. High-Accuracy Simultaneous Calibration of Signal Measuring Systems. Meas. Sci. Technol., v. 1, 1990, pp. 225-230.

40. Sternberg, B. K., T. M. Ryan, J. W. McGill, and M. E. Breitrick. The San Xavier Geophysics and Tunnel-Detection Test Site. Lab. Adv. Subsurf. Imaging, Univ. AZ Dept. Min. and Geol. Eng., LASI 88-2, July 6, 1988, 134 pp.

41. Sternberg, B. K., J. C. Washburne, and L. Pellerin. Correction for the Static Shift in Magnetotellurics Using Transient Electromagnetic Soundings. Geophysics, v. 53, No. 11, 1988, pp. 1459-1468.

42. Tweeton, D. R., C. L. Cumerlato, J. C. Hanson, and H. L. Kuhlman. Predicting and Monitoring Leach Solution Flow With Geophysical Techniques. Paper in In Situ Leach Mining. BuMines IC 9216, 1989, pp. 83-84.

43. Ward, S. H., and G. W. Hohmann. Electromagnetic Theory for Geophysical Applications. Ch. 4 in Electromagnetic Methods in Applied Geophysics, v. 1, Theory, ed. by M. N. Nabighian. Soc. Explor. Geophys., 1988, pp. 131-311.

44. Warner, B. N., M. G. Bloomquist, and P. G. Griffith. Magnetotelluric Interpretations Based Upon New Processing and Display Techniques. Paper in 1983 Technical Program. Expanded Abstracts With Biographies (53d Annu. Int. Meet., Las Vegas, NV, Sept. 11-15, 1983). Soc. Explor. Geophys., 1983, pp. 151-154.

45. Wayland, J. R., D. O. Lee, S. M. Shope, and K. L. Zonge. Electromagnetic Geophysical Tunnel Detection Experiments—San Xavier Mine Facility, Tucson, AZ. Sandia Nat. Lab. Rep. SAND91-0053, 1991, 32 pp.

46. White, P. A. Measurement of Ground Water Parameters Using Salt-Water Injection and Surface Resistivity. Ground Water, v. 26, No. 2, 1988, pp. 179-186.

47. Zonge, K. L., and L. J. Hughes. Controlled Source Audio-Frequency Magnetotellurics. Ch. 9 in Electromagnetic Methods in Applied Geophysics, v. 2, Application, ed. by M. N. Nabighian. Soc. Explor. Geophys., 1991, pp. 713-809.